J. Fluid Mech. (2013), *vol.* 737, *pp.* 19–55. © Cambridge University Press 2013
doi:10.1017/jfm.2013.541

High-speed laminar flow past a fin–body junction

O. R. Tutty†, G. T. Roberts and P. H. Schuricht

Engineering and the Environment, University of Southampton, Highfield, Southampton SO17 1BJ, UK

(Received 23 January 2013; revised 30 August 2013; accepted 9 October 2013;
first published online 15 November 2013)

Interference heating effects generated by a blunt fin-type protuberance on a flat plate exposed to a hypersonic flow have been investigated experimentally and numerically. Experiments and simulations were carried out at a free-stream Mach number of 6.7 under laminar flow conditions. The surface heating on the plate was measured experimentally using liquid-crystal thermography, which provided quantitative data with high spatial resolution. Complementary surface oil flow and schlieren experiments were also carried out to gain a better understanding of the interference flow field. The effects of fin leading-edge diameter on the heating distribution on the flat plate surface were explored. The results of the experiments and simulations agree well and reveal a highly complex interaction region which extends over seven diameters upstream of the fin. Within the interaction region surrounding the fin, heating enhancements up to ten times the undisturbed flat plate value were estimated from the experimental data. However, the liquid crystals have a limited range, and the numerical simulations indicated localized peak heating many times this value both on the plate and the fin itself.

Key words: high-speed flow, shock waves

1. Introduction

One of the fundamental design requirements of hypersonic and other high-speed vehicles is the capability to withstand the severe aerodynamic heating experienced at those speeds. The areas usually of most concern are stagnation regions and, in the case of complex flows involving flow separation, areas of attachment. Flow separation is a common consequence of shock–boundary layer interactions caused, for example, by ramps, flaps, fins or jets used as vehicle control mechanisms. The interference effects created by shock–boundary layer interactions are not necessarily localized and have a profound effect on the heating distribution on the vehicle surface and on the overall aerodynamic performance of the vehicle.

Shock–boundary layer interactions have been studied over the past five decades or more. Reviews of the literature can be found in e.g. Delery & Marvin (1986), Dolling & Bogdanoff (2001) and Babinsky & Harvey (2011). As a result, much is understood about the general characteristics of these flow fields. However, in three-dimensional flows involving shock–boundary layer interactions the flow features are complex and difficult to predict *a priori*, particularly the pattern of heating and maximum heat flux

† Email address for correspondence: o.r.tutty@soton.ac.uk

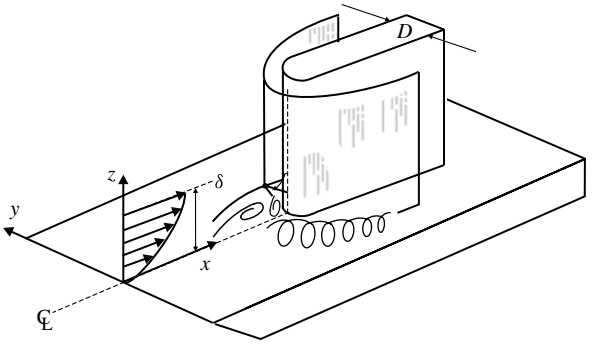

FIGURE 1. Blunt fin interaction schematic (after Hung & Buning 1985).

in the interaction region. Consequently, it remains necessary to carry out experimental or numerical studies in order to determine the exact nature of the flow under given geometric and/or flow conditions.

Often generic-type flow fields involving shock–boundary layer interactions are studied in order to simplify the problem and to elucidate the flow features and their origins. One such flow field is that created by a blunt fin on a flat plate exposed to a supersonic or hypersonic free-stream flow. This type of geometry is a simplified representation of a wing–body or fin–body junction on a high-speed vehicle. Reviews of past work with this geometry can be found in Holden (1986) and Stollery (1989). Sometimes, instead of a fin, a cylindrical protuberance is studied (e.g. Dolling & Bogdanoff 1981); the flow upstream of both types of protuberance is similar although differs as the flow expands around the side. In either case the flow features have mostly been inferred from surface measurements of pressure or heat transfer, or by visualization techniques such as schlieren photography and surface oil flow. As such, although some features of the flow field may be deduced, the detail often remains uncertain, particularly of the three-dimensional flow above the surface.

Figure 1 illustrates the geometry and typical flow field features exhibited by a blunt fin on a flat plate in supersonic or hypersonic flow. The bow shock surrounding the fin interacts with the oncoming boundary layer growing over the flat plate. The pressure rise across the shock is transmitted upstream through the subsonic portion of the boundary layer. If it is strong enough, the retardation of the flow in the boundary layer will lead to flow reversal, and hence separation. The deflection of the free-stream flow caused by the separated boundary layer in turn forms a secondary, separation shock wave that interacts with the bow shock. At this intersection, known as a triple point, there is a lambda-type shock structure consisting of the incident separation shock, and the two arms of the bow shock above and below the intersection, the lower arm being deflected by the shock–shock interaction (Dolling & Bogdanoff 1982). In fact, in the current work, the complex nature of the flow in the separation region gives rise to a number of secondary shocks, and hence to multiple shock–shock interactions and triple points.

The separated flow upstream of the fin rolls up into a series of horseshoe vortices as it expands around the side of the fin. Within the separated flow region there is a mixture of subsonic and supersonic flow with embedded shock waves. Areas of enhanced heating and pressure are experienced on the plate surface and the fin itself. In both cases the peak heating is typically much higher than the undisturbed value,

i.e. the values that would be found on a plate without a fin or a fin without a plate. Factors that govern the scale of the interaction zone and amplitude of the enhanced pressure and heating within it are the diameter and height of the fin and its angle of sweep and incidence, as well as the state and thickness of the upstream boundary layer, the last being governed by the Reynolds number of the flow (Dolling & Bogdanoff 1981).

In general terms, the description of the flow outlined immediately above applies when the incoming boundary layer flow on the plate is either laminar or turbulent, although the details of the flow differ significantly, including the size of the fin–body interaction region, depending on the state of the flow in the boundary layer. Although by far the majority of previously published work has considered turbulent boundary layer interactions, laminar interactions remain of interest since high-Mach-number flows are resistant to transition (see e.g. Anderson 1989), and a hypersonic vehicle (e.g. one re-entering the Earth's atmosphere) may spend a significant duration of its flight time at high altitude where, despite the high speed, the unit Reynolds number is sufficiently low to maintain laminar flow. However, it should be noted that shock–boundary layer interactions can provoke transition, although again there is evidence to suggest that transition is delayed at high Mach number (e.g. Yao, Sandham & Roberts 2007).

Hung & Clauss (1981) demonstrated that the upstream extent of separation ahead of an unswept cylindrical protuberance at a Mach number of 5.3 was dependent on the cylinder diameter and height. For cylinders of heights greater than a certain value (known as the asymptotic height) the separation distance was only dependent on the cylinder diameter, D, and state of the boundary layer. For cylinders greater than the asymptotic height, Hung & Clauss (1981) found that for turbulent interactions the separation distance was $2.5D$–$3D$, whereas for laminar interactions it was $9D$–$12D$. The larger separation distance, and hence greater extent of the interaction zone, in the laminar case is the result of the laminar boundary layer being less tolerant to adverse pressure gradients and hence more prone to separation. Some controversy exists over the asymptotic height but Dolling & Bogdanoff (1982) indicate that it is achieved when the height of the fin is 2–3 times the height at which the separation shock intersects the fin bow shock (the triple point). At lower heights the separation distance is reduced.

Hiers & Loubsky (1967) studied the heating in the vicinity of the leading edge on a fin mounted on a flat plate with laminar flow. The flat plate was placed at an angle to the Mach 14 free-stream flow to generate a shock that impinged on the fin bow shock, their main interest being the heating due to the resultant shock–shock interaction. Peak heating several times the undisturbed stagnation value was recorded, although given the limited spatial resolution of the measurement technique it is quite likely that this was an underestimate of the peak heating experienced on the fin leading edge. The peak heating recorded occurred near the intersection of the shock generated by the plate with the fin bow shock. The enhanced heating in that area was attributed to impingement of a vortex sheet, resulting from the shock–shock interaction, on the leading edge of the fin.

Haq (1993) also observed large heating on the side of an unswept blunt fin on a flat plate with a turbulent boundary layer in a Mach 6.2 flow; indeed the leading edge of the fin was damaged by the excessive heating in the area near the triple point. Perhaps the most well-known example of this type of heating is that experienced on a pylon carrying a dummy ramjet engine on one of the last flights of the X-15 experimental vehicle at Mach 6.7. As a result of the intense heating, subsequently attributed to a

shock–shock interaction ahead of the pylon, the skin of the pylon was burnt through in several places and the ramjet model was lost in flight (Burcham & Nugent 1970).

The investigations referred to above are mainly experimental in nature. To date rather few numerical studies of the flat plate–blunt fin flow field have been performed. One of the earliest was carried out by Hung & Buning (1985) at Mach 2.95 with a turbulent boundary layer. The results were compared with the experimental data of Dolling & Bogdanoff (1982) for an unswept fin. The pressure field on the stagnation line of the fin and also on the flat plate surface were reasonably well-simulated, although the peak pressures were under-predicted. This was thought to be due to limited mesh resolution.

Tutty *et al.* (1994) also carried out turbulent blunt fin–plate simulations, comparing their results with the Mach 6.2 heat transfer data obtained by Haq, Roberts & East (1991). Note that accurate simulation of heat transfer is much more challenging than that of the pressure field because of the dependence of the former on gradient properties, requiring good grid resolution. The general characteristics of the flow field appeared to be well-simulated, but the rise in heat flux ahead of the fin was predicted to occur ahead of the location observed in the experiments; again this was attributed to limited grid resolution. Nevertheless the heat flux distribution ahead of the fin was reasonably well-simulated with a peak heat flux of 25 times the undisturbed (flat plate) value being predicted near the base of the fin; this value was much higher than could be recorded in the experiments.

Lakshmanan & Tiwari (1994) investigated numerically a laminar blunt fin–flat plate flow field at various Mach numbers and unit Reynolds numbers. They predicted that the extent of upstream separation increased with increasing unit Reynolds number, but decreased with Mach number, and that the number of vortices present in the separation zone upstream of the fin was dependent on both the free-stream Mach number and unit Reynolds number.

Numerical simulations of a laminar blunt fin–flat plate interaction are reported in Houwing *et al.* (2001). In this case the numerical simulations were carried out to help interpret the results of flow visualization experiments carried out under high-enthalpy, high-Mach-number conditions. The simulations appeared to provide a reasonable prediction of the temperature field in the separation zone upstream of the fin as well as the overall flow characteristics in that region.

This paper presents the results of high-resolution numerical simulations of a laminar blunt fin/flat plate flow field at Mach 6.7, with a much finer grid than previous investigations (e.g more than two orders of magnitude more grid points than that used by Lakshmanan & Tiwari 1994). This enables a much more detailed comparison with complementary experiments with the same configuration and flow parameters than attempted previously. The fin is unswept and at zero incidence with respect to the oncoming free stream. A steady-state solution was obtained in the simulations. The effect of leading-edge diameter is explored both experimentally and numerically. Below, details of the experimental facility and protocol are given (§ 2), followed by an outline of the numerical method (§ 3). The flow past the thickest fin (7.5 mm) is then considered (§ 4), with a detailed comparison of the surface heat flux from the experiments, as measured using a high-spatial-resolution technique (Schuricht & Roberts 1998), with the numerical predictions. The experimental measurements provide a picture of the heating distribution over the entire surface of the flat plate that the fin is mounted on, in contrast to other measurements found in the research literature which are confined to isolated measurements along the centreline upstream of the body. In general, good agreement is found between the numerical predictions

P_0	12.5 bar	P_∞	398 Pa
T_0	630 K	T_∞	63 K
M_∞	6.7	U_∞	1084 m s^{-1}
Re	5.0×10^6 m^{-1}		
Run time	~0.5 s		
Boundary layer	Laminar		

TABLE 1. SULPIC Operating conditions. The values on the left are those for the tunnel and those on the right are the matching values as used for the inflow in the numerical work.

and experimental measurements. This section also contains an investigation of the off-surface flow, using the flow fields generated numerically, which provide a far more detailed description of the flow than could be obtained through experimental measurements. The following section (§ 5) considers the effect of the fin thickness on the flow, with a summary and conclusions in the final section (§ 6).

2. Experimental details

2.1. *Experimental facility*

The experiments, against which the numerical results are compared, were carried out in the Southampton University light-piston isentropic compression (SULPIC) hypersonic wind tunnel. This facility, which has now been decommissioned, provided a steady flow of ~0.5 s duration at a modest stagnation temperature and was thus well-suited to the liquid-crystal thermographic technique used in this study. The design and operation of the facility have been detailed elsewhere (Qaswari 1977). In the present case, the run conditions were as specified in table 1. The test gas was nitrogen. Under these conditions, comparison with predictions of the surface heat transfer rate from the Eckert correlation show that the boundary layer in in the undisturbed region on the flat plate ahead of the fin is laminar (see §§ 4 and 6 below).

2.2. *Model design*

The model comprised a zero-incidence steel flat plate, 205 mm long and 102 mm wide, with a sharp leading edge. A single unswept blunt fin, 60 mm in length, was located approximately 145 mm from the plate leading edge (to allow a substantial boundary layer to develop ahead of the fin) and offset from the centreline by approximately 25.5 mm (to allow a large heating footprint to be observed). The fins all had a hemi-cylindrical leading edge, but with different thicknesses (figure 2). The thickest fin (7.5 mm) is taken as the baseline configuration as this gives the best resolution in terms of pixel size in the imaging (see below) with respect to the fin size. The height of the fin (25 mm) was sufficient to satisfy the asymptotic criterion suggested by Dolling & Bogdanoff (1981) so that its height did not affect the heating magnitude or distribution on the flat plate (this was tested numerically and found to hold; see § 3 below).

For the surface oil flow tests the surface of the plate was coated with a thin layer of titanium dioxide particles suspended in a silicon (vacuum compatible) oil. The viscosity of the particle/oil slurry was adjusted so that it flowed smoothly during a tunnel run (indicating regions of high and low surface shear) but did not accumulate or run excessively, thus preventing disturbances to the flow.

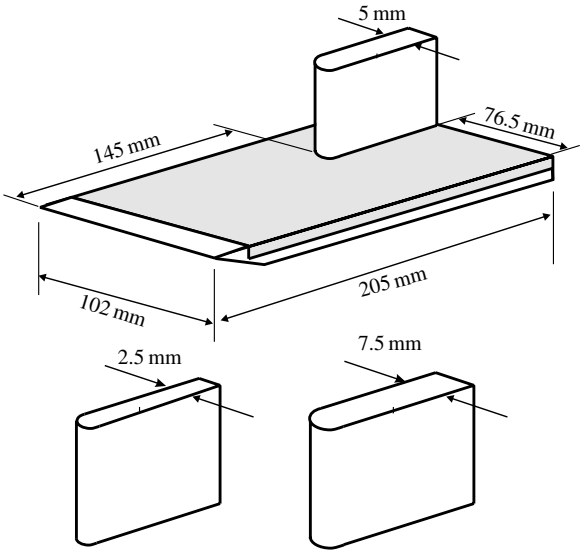

FIGURE 2. Model schematic.

Liquid-crystal thermography (Roberts & East 1996) was employed to obtain quantitative estimates of the heat flux distribution on the flat plate in the vicinity of the fin–plate interaction zone (see the next section). For the heat transfer tests, an insert of plastic (Delrin) was incorporated into the model with its surface flush with that of the metal (shown in grey on figure 2) to maximize the surface temperature rise during the run. The depth of the plastic (2 mm) was chosen to ensure that it remained effectively semi-infinite throughout the duration of the run, so far as the non-steady heat pulse is concerned (Schultz & Jones 1973). The initial temperature of the model (measured by a K-type thermocouple embedded within the plastic) was regulated by an integral heating/cooling system comprising channels through which hot or cold water could flow; this also permitted *in situ* calibrations of the liquid crystals to be performed. The model was sprayed with a thin layer of black backing paint (Hallcrest type BB-G1) to remove any colour bias from the plastic layer before the liquid crystals (Hallcrest type BM/R30C6W/C17-10) were applied by air spray. The response of the liquid crystals to changes in temperature is reversible and repeatable; therefore, in principle, the liquid crystals can be used repeatedly for many runs. However, in the experiments reported here, the liquid crystal layer became ablated near the root of the fin at its leading edge (due to the high shear and heat flux that is experienced in this region) and so the flat plate was frequently stripped clean and re-sprayed with black paint and liquid crystals (usually after every 5–6 runs).

2.3. *Heat flux measurement technique*

The use of liquid-crystal thermography in short-duration hypersonic wind tunnel facilities has been reviewed in Roberts & East (1996). This technique had been used previously in the SULPIC facility to investigate heating caused by fin/flat plate interactions under turbulent flow conditions (Haq *et al.* 1991) and also transverse jet interactions under laminar flow conditions (Roberts, Schuricht & Mudford 1998). The method employed in the present study of laminar flat plate/fin interactions is somewhat different to that employed by Haq *et al.* (1991) and so warrants some explanation.

When illuminated with white light, thermochromic liquid crystals respond to changes in temperature by changing colour progressively from red through to blue as their temperature increases. The range of temperatures over which the liquid crystals are colour active is limited, but can be tailored (by the manufacturer) to suit a particular application. Below the red-start temperature the liquid crystals are colourless and transparent; upon heating through the blue colour range they eventually become colourless and transparent again. The so-called colour-play range or bandwidth is usually characterized by the red-start to blue-start temperatures, since the blue-colour temperature range is usually broad and the colour change in that range only a weak function of temperature. Monitoring the colour of the liquid crystals can, in principle, give an indication of the underlying surface temperature and hence a measure of the heat flux the surface is experiencing. The liquid crystals had a red-start to blue-start bandwidth of approximately 6 °C with a red-start temperature of 30 °C. The colour–temperature calibration (see below) extended slightly into the blue colour range and so the range of surface temperatures deduced from the liquid-crystal response was approximately 30°C–38°C.

The thermal response of the plate to the suddenly applied aerodynamic heating was monitored by recording the colour change of the liquid crystals on videotape using a Hadland photonics high-speed video system. A strobe was used to illuminate the image during capture. This had an exposure time of 20 μs. The liquid-crystal response time is typically ∼3 ms, so that the liquid-crystal response is effectively frozen on the images obtained (Roberts & East 1996). The images were captured at a rate of 50 frames s^{-1} and so, typically, ∼25 frames were recorded per run. These were then digitized using a PC-hosted imaging technology colour frame grabber. The red, green and blue (RGB) intensity values for each of the 256 × 256 pixels in the images were converted to hue, saturation and intensity (HSI) values; in this coordinate system, the hue value is an angular representation of colour (Roberts & East 1996). Therefore, by monitoring the hue exhibited by the liquid crystals as the model was heated by the flow during the run the temperature distribution on the model in each image could be determined.

To achieve this, calibrations were performed *in situ* under the same optical conditions as in the experiments by heating the plate in the SULPIC facility and allowing it to cool naturally whilst simultaneously monitoring the hue and temperature. A polynomial curve-fit was applied to the derived hue versus temperature relation and subsequently used to estimate the surface temperature for a measured value of hue. Calibrations were carried out on a regular basis (particularly after re-spraying) to minimize the effects of changes in optical or data acquisition parameters and any variation in response of the liquid crystals to surface temperature changes. The calibration data were spatially averaged over a 15 × 15 box of surrounding pixels to remove noise. This gives an uncertainty of ±0.1°C in the calibration data, as compared with ±1°C for a single pixel. However, temporal averaging can be used to reduce the uncertainly when using individual pixels (see below).

From the measured surface temperatures, the heat flux $\dot{q}$ can be evaluated directly from the solution to the equation for one-dimensional non-steady heat conduction at the surface of a homogeneous, semi-infinite substrate (Schultz & Jones 1973)

$$\Delta T = T(t) - T_i = \frac{2}{\sqrt{\pi}}\,\dot{q}\,\sqrt{\frac{t}{\rho c k}} \tag{2.1}$$

where $T(t)$ is the surface temperature measured by the liquid crystals, T_i the initial surface temperature, measured using the thermocouples embedded in the plastic

(typically $T_i \sim 30°\mathrm{C}$, i.e. at or just below the liquid crystal red-start temperature), and ρ, c and k are the density, specific heat capacity and thermal conductivity of the solid, respectively. The Delrin material used here has a thermal product $\sqrt{\rho c k} = 880\ \mathrm{J\ m^{-2}\ K^{-1}\ s^{-1/2}}$. In using (2.1), it has been assumed that the thin ($\sim$20 μm) layer of liquid crystals and black paint had a negligible effect on the thermal response of the model surface (this is likely to be the case as the thermal product of the liquid crystals and paint is similar to that of the underlying plastic material).

Equation (2.1) ignores lateral conduction effects and applies only if the heat flux remains constant with time. In practice the latter requires the measured surface temperature rise to be small compared with $T_a - T_i$ where T_a is the adiabatic wall temperature. For the undisturbed flat plate flow

$$T_a = T_\infty(1 + r(\gamma - 1)M_\infty^2/2) \tag{2.2}$$

where r is the recovery factor, equal to $\sqrt{Pr}$ for laminar flow. For nitrogen, at the temperatures of interest in this work, the Prandtl number Pr is 0.704 and γ, the ratio of specific heats, is 1.4. Using the free-stream conditions (table 1), for a flat plate, T_a is approximately 540 K, so that $T_a - T_i$ is greater than 200 K. Since the active range of the liquid crystals used in this work is only 8 K, the assumption of small temperature change compared with $T_a - T_i$ is satisfied.

In principle, it is possible to evaluate the heating distribution in the interaction region from a just single image (provided the liquid crystals are everywhere active). However, in the images obtained there were usually areas where either the crystals had not become active (in regions of low heat flux) or may have passed through the active bandwidth (in regions of high heat flux), depending on the initial temperature of the model and the time elapsed after start of the run. In both cases, data from these regions were rejected by incorporating an intensity threshold (where all pixels with a light intensity corresponding to the black model with inactive crystals were ignored) and a hue threshold (where all pixels with a hue value outside the active bandwidth were ignored). To obtain the maximum range of valid data, at a given pixel location data from different frames were merged by plotting the evaluated ΔT values against $\sqrt{t/\rho c k}$: according to (2.1) the gradient of the straight line that should result will give the value of $\dot{q}$ averaged over all the images. This procedure has the added advantage that the effects of random noise on the data (usually a result of the digitization of the video images) are much reduced. An estimate of the heat flux could be made with as few as three frames, taking 0.06 s from the start of the run. However, in regions of very high heat flux the liquid crystals transitioned through their active temperature range very quickly and so were unable to provide a reliable estimate of the peak heating in those regions, although a lower bound could nevertheless be estimated.

Figure 3(*a*) shows a photographic image of the liquid-crystal response for the 5 mm fin, taken approximately 0.3 s after the start of the run. It should be noted that the spatial resolution in this image is higher than those digital images obtained via the frame grabber, which had a pixel size of approximately 0.9 mm × 0.6 mm. The change in surface temperature between the relatively cool steel surface and warm plastic surface is clearly visible as the vertical line near the leading edge, towards the left of the image. Surrounding the fin is a complex heating distribution, evident by the patterns displayed by the liquid crystals. The bands in the image indicate regions of low or high heat flux and correspond to lines of separation or attachment, respectively, of the vortical flow surrounding the fin. Near the fin itself, where the heat flux is

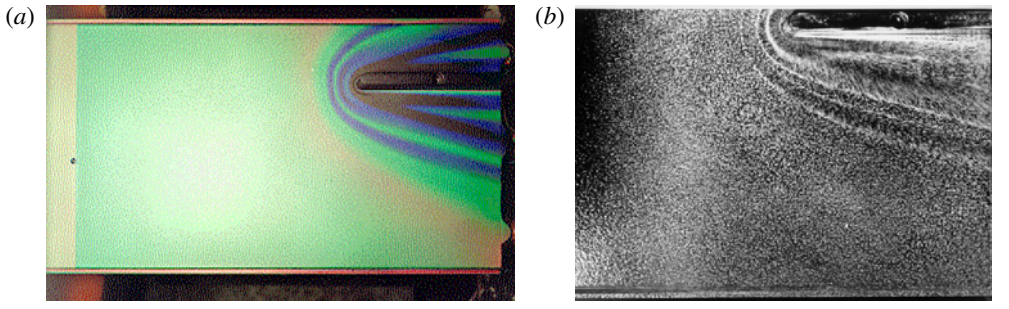

FIGURE 3. (Colour online) (*a*) Liquid-crystal response and (*b*) oil flow results for the 5 mm fin.

highest, there are black bands in the image, showing regions where the heat flux is such that the liquid crystals have cleared, with the surface temperature rise in excess of the colour-play temperature range. Figure 3(*b*) shows a photographic image of the oil flow pattern obtained for the 5 mm fin. Accumulations of oil in regions of low shear and absence of oil in regions of high shear are clearly visible. There is a clear similarity between the patterns displayed by the oil flow and those obtained from the liquid crystals. The distribution of heating will be discussed below in §§ 4 and 5, where both the experimental and numerical results are explored in detail.

From the experimental measurements, a map of the heat flux on the plate can be constructed, pixel by pixel. These data are presented below using a red-to-blue/low-to-high colour map, with areas where an estimate could not be made shown as white. The numerical results are presented using a similar colour map. Red-to-blue was chosen rather than the more conventional blue-to-red/cold-to-hot map for two reasons. First, it reflects the red-to-blue behaviour of the liquid crystals, and, second, visually it gives a better presentation of the pattern of heat flux on the plate.

2.4. *Accuracy of results*

Eckert (1955) gives a semi-empirical correlation which gives reliable estimates of the surface heat flux and shear stress for a flat plate (τ_{wp}). First, calculate the skin friction coefficient $C_f = \tau_{wp}/(\rho_\infty U_\infty^2/2)$ from

$$C_f = 0.664\sqrt{\frac{\rho^*\mu^*}{Re_x\,\rho_\infty\mu_\infty}}, \tag{2.3}$$

then the heat flux $\dot{q}_p$ from

$$\dot{q}_p = \tfrac{1}{2}\rho_\infty U_\infty c_p(T_a - T_w)Pr^{-2/3}C_f. \tag{2.4}$$

Here Re_x is the Reynolds number based on the free-stream (∞) values and the distance from the leading edge of the plate, T_w is the temperature of the wall, $\rho_w = P_\infty/RT_w$ and μ_w are the density and viscosity at the wall, R is the gas constant, c_p the specific heat of the gas, and ρ^* and μ^* the density and viscosity of the gas at the boundary layer intermediate temperature

$$T^* = \tfrac{1}{2}(T_w + T_\infty) + 0.22(T_a - T_\infty). \tag{2.5}$$

A comparison of the results obtained for a flat plate with no fin with the Eckert correlation has shown agreement for the heat flux within a range of uncertainty

of $\pm 10\,\%$ under the present experimental conditions (Roberts & East 1996). In this case the uncertainty arises mainly from random fluctuations in the surface temperature deduced from the liquid-crystal response due to noise on the video images although, as noted above, the net result of such effects is minimized by merging data from multiple images. This uncertainty is larger than would typically be obtained with more conventional, discrete, heat flux gauges (Schultz & Jones 1973), but the spatial coverage and resolution of the liquid crystals is much superior, which makes them well-suited to this present application.

However, the undisturbed flat plate is the best case in terms of the expected errors. The uncertainty will be worse in the interaction region around the fin where fewer frames are used because of high heat fluxes. The data are presented below pixel by pixel without spatial averaging, as pixel averaging was found to obliterate fine features of the flow in this region. The data were checked for cross-conduction between pixels (Schultz & Jones 1973). This was in general limited to pixel-type dimensions, although will be worse in regions with high temperature gradients. Again, this could lead to a lack of definition in regions with high gradients, in particular, along the symmetry line ahead of the fin.

The limited temperature range of the liquid crystals implies a limit on the heat flux that can be measured. The active temperature bandwidth for the liquid crystals used in this study was approximately 8 K, and the minimum time required to record three frames of data was 0.06 s. Hence, the maximum heat flux that could be measured is estimated from (2.1) to be $\dot{q}_{max} = 2.6 \times 10^4$ W m^{-2}. However, under high heat flux conditions ($\dot{q} \gg 10^4$ W m^{-2}) the liquid crystals not only transition through their active colour-play bandwidth very quickly, but the colour response is skewed by the steep temperature gradient within the liquid-crystal layer (Roberts & East 1996), causing the hue–temperature calibrations, which were obtained under low heat flux conditions, to become invalid.

In §§ 4 and 5 below, the Eckert flat plate formulae (2.3) and (2.4) are used to normalize the experimental and numerical data, in particular, to compare the heat flux on the flat plate with the fin ($\dot{q}$) to that on the undisturbed flat plate with no fin ($\dot{q}_p$). Both the skin friction and the heat flux from the Eckert formulae have the usual $x^{-1/2}$ behaviour found with laminar boundary layers. Because of the limited range of heat fluxes that could be estimated experimentally, the maximum normalized heat flux ($\dot{q}_{max}/\dot{q}_p$) that can be estimated varied along the plate surface. For the test conditions, with a temperature range of 8 K and a minimum sample time of 0.06 s, (2.1) and (2.4) imply a range of $\dot{q}_{max}/\dot{q}_p$ from $\sim$4 near the leading edge of the plate to over 10 near the base of the fin and further downstream. However, as noted above, the hue–temperature calibration becomes invalid at high heat fluxes. The effect of this is difficult to quantify, but comparison of the numerical and experimental results suggests that estimates of $\dot{q}/\dot{q}_p$ are reliable for only about half the maximum value, the liquid-crystal technique underestimating the true values at higher heat fluxes. Fortunately the majority of the heat fluxes on the flat plate are sufficiently low for reliable estimates to be made, except in certain localized regions of the fin–body interaction zone where the heat fluxes are very high. In these regions non-dimensional heating rates up to around 10 were estimated from the experimental data; even though these are an underestimate of the true values the experimental data were retained in the plots presented below as they do indicate regions of high heat flux and the map of the surface heat flux distribution gives a good indication of the behaviour of the flow near the surface of the plate.

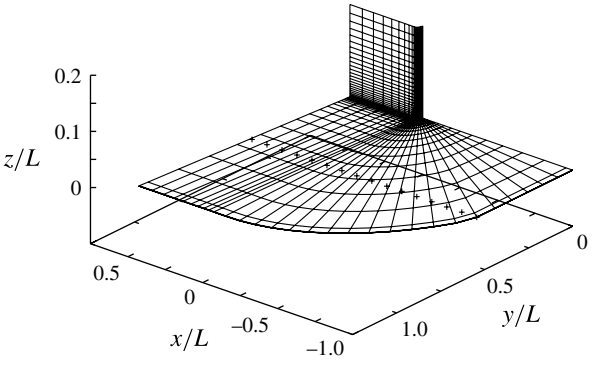

FIGURE 4. A three-dimensional view of a coarse version of the grid. The symbols denote the edge of the plate in physical space. $L = 0.145$ m.

On the fin, the heat flux that would be found on the stagnation line on the leading edge for an undisturbed flow, i.e. for two-dimensional flow normal to an infinite length fin, provides an alternative reference heat flux value to the flat plate Eckert value. This will be discussed further in the next section, but, for a 7.5 mm diameter fin, this heat flux is approximately 2×10^5 W m^{-2}, around eight times $\dot{q}_{max}$ for a sample time of 0.06 s. For this reason, the liquid-crystal technique was not used to measure the heat flux on the fin.

3. Numerical scheme

The equations solved are the three-dimensional compressible Navier–Stokes equations, in standard conservation form, with the equation of state being that for an ideal gas. The viscosity μ is obtained using Lennard–Jones potentials, as in Amaratunga, Tutty & Roberts (2000) and Navarro-Martinez (2002). The conductivity of the gas is related to the viscosity through a constant Prandtl number of 0.704.

Isothermal no-slip conditions were applied at the surface of the plate and the fin, with wall temperature $T_w = 300$ K. The flow was assumed to be symmetric along the centreline upstream of the plate ($y = 0$, figure 4). The experimental configuration (§ 2.2) had the model offset from the centre of the plate in order to provide a large heating footprint. However, as shown by the surface heat flux distribution (figure 3), there is no discernible transverse effect from this displacement near the fin, justifying the assumption of symmetry in the calculations. Outflow boundary conditions were applied in the rest of the domain boundary surfaces except at the inflow which was placed 5 grid points ahead of the leading edge of the plate, where free-stream values were imposed. An initial flow field was generated on a relatively coarse grid, starting from a flow at rest at wall temperature. For finer grids, starting values were generated by interpolation from existing converged solutions.

The code used here is based on a well-validated code used in a number of previous studies on hypersonic flow (Navarro-Martinez 2002; Navarro-Martinez & Tutty 2005). In the original code, the inviscid fluxes are obtained using Godunov's method with the three-wave HLLC approximate Riemann solver (Toro, Spruce & Speares 1994). An extension to higher order away from shocks is obtained through a MUSCL slope-limiting approach (van Leer 1979), preserving the monotonicity and conservativity of the solution for non-centred grids. The Minmod slope limiter has been implemented

with a parameter ε to control the degree of slope limiting (see Amaratunga *et al.* 2000 for details). For all the calculations presented here, $\varepsilon = 0.95$, the maximum value consistent with numerical stability. A second-order Runge–Kutta method was used to time march the solution to a steady state. The time step was set by setting the CFL number to 0.75. Wall shear stress and heat transfer values were monitored to ensure that a steady state had been achieved.

Calculations performed using the code as outlined above showed unexpected, non-physical, behaviour along the line of symmetry upstream of the fin. This was due to a well-known effect, known as the 'carbuncle phenomenon' (Quirk 1994). It is a numerical effect which can occur when a shock wave is aligned with the grid, although usually in inviscid flow. Here it appeared in the region of the root of the separation shock (the separation point along the centreline is at $x/D \approx -6.5$). The standard 'fix' is to use a more dissipative method for the inviscid part of the calculation. One such method is the Rusanov scheme (Rusanov 1961), which is known to be 'carbuncle-free'. In the current application, if applied over the whole flow field, the Rusanov scheme gives a less accurate solution, i.e. for most of the flow, one similar to that obtained using the HLLC flux with fewer grid points. Accordingly we use a hybrid Riemann solver which blends both the HLLC and Rusanov fluxes. Let

$$\alpha = \frac{\Delta \boldsymbol{v} \cdot \boldsymbol{n}}{|\Delta \boldsymbol{v}|} \tag{3.1}$$

where $\boldsymbol{n}$ is the unit normal to and $\Delta \boldsymbol{v}$ the change in velocity across the cell face where the Riemann solver is applied (if $|\Delta \boldsymbol{v}| = 0$, $\alpha = 0$). The inviscid flux is given by

$$\boldsymbol{F}_h = \alpha^2 \boldsymbol{F}_R + (1 - \alpha^2) \boldsymbol{F}_{HLLC} \tag{3.2}$$

where $\boldsymbol{F}_R$ and $\boldsymbol{F}_{HLLC}$ are the Rusanov and HLLC fluxes respectively. If the change in velocity is normal to the cell face then $\alpha = 1$ and the Rusanov flux is used, but for a non-normal (or zero) change the flux is essentially that from the HLLC solver. This produced a solution which is carbuncle-free but, away from the line of symmetry, almost the same as that obtained using the HLLC flux only.

A boundary-fitted curvilinear grid was used, mapping (x, y) to a rectangular grid (η, ζ), with, as shown in figure 4, essentially a polar grid around the nose of the fin and a Cartesian grid along the side of the fin. In this figure, η runs outward from the fin and ζ along the fin, with $\zeta = 0$ the far-field boundary and $\zeta = 1$ along the surface of the fin, $\eta = 0$ the symmetry line ahead of the fin and $\eta = 1$ the downstream boundary. Grid points in η along the symmetry line were clustered near the fin and the leading edge of the plate where the largest variations in the flow were expected. There is a simple stretching of the grid normal to the plate, with a ratio of approximately 77 at $z = z_{max}$ to one at the surface.

Figure 4 also shows the position of the transverse edge of the plate at $y = 79$ mm. Points with $y \leqslant 79$ mm have isothermal no-slip conditions, while those with larger y have symmetry conditions imposed there, as for the points upstream of the plate. To test the effect of the position of the transverse boundary of the plate, a calculation was performed with solid isothermal wall conditions extended laterally, with a halo of 5 grid points at the edge with symmetry conditions, as for the flow upstream of the plate. Not surprisingly given the Mach number of the free stream, there was no significant difference in the flow except at and beyond the lateral edge of the plate. In particular, the surface heating and shear stress did not change significantly up to a few points from $y = 79$ mm.

Grid	N_η	N_ζ	N_z	x_s/D
G_1	96	88	80	−5.81
G_2	288	176	160	−6.76
G_3	384	176	160	−6.66
G_4	480	176	160	−6.61
G_5	576	176	160	−6.55
G_6	672	176	160	−6.52
G_7	672	176	240	−6.53
G_8	384	264	240	−6.67

TABLE 2. Number of grid points and the primary separation point for the 7.5 mm fin.

A number of different grids were used, as listed in table 2, where N_η, N_ζ and N_z are the number of points in the corresponding direction. The grid with the fewest points, labelled G_1, is too coarse to resolve the details of the vortex structure near the fin/plate junction, but it provides a reasonable approximation for the shock structure. The solution on grid G_1 was used as the starting point for calculations on successively finer grids, interpolation between grids being more efficient than starting every calculation from scratch.

For most of the calculations, $z_{max} = 25$ mm, matching the height of the fin in the experiments. However, a calculation was performed with a fin up to $z = 45$ mm by adding extra points in z to the G_7 grid. There was no significant difference to the flow in the fin–body interaction zone. The top 15 mm of the extended fin is above the point where the leading-edge shock impinges on the bow shock. The flow here is essentially two-dimensional with a uniform flow approaching the fin until it encounters the bow shock. Values from this relatively simple flow can be used as a basic check on the results generated by the numerical procedure. Amick (1961) gives the stand-off distance S for the bow shock along the line of symmetry upstream of a cylinder in supersonic flow as

$$\frac{S}{D} = 0.19 + \frac{1.2}{M_\infty^2 - 1} + \frac{0.7}{(M_\infty^2 - 1)^2}. \tag{3.3}$$

For $M_\infty = 6.7$ this gives $S/D = 0.22$. The same stand-off distance was obtained in the numerical solution for the top part of the fin. A number of semi-empirical formulae which predict the surface heat flux ($\dot{q}_f$) on the stagnation line at the front of a cylinder can be found in the literature. For the flow conditions here, for a 7.5 mm diameter fin, from Fay & Riddell (1958) we obtain $\dot{q}_f = 1.86 \times 10^5$ W m^{-2}, from Anderson (1989) $\dot{q}_f = 1.92 \times 10^5$ W m^{-2}, and from Hayes & Probstein (1959) $\dot{q}_f = 2.14 \times 10^5$ W m^{-2}. The numerical solution with the extended fin produced $\dot{q}_f = 2.0 \times 10^5$ W m^{-2}, consistent with the semi-empirical predictions. Note that the predicted heat fluxes will vary as $D^{-1/2}$, with larger heat fluxes on smaller diameter fins.

Table 2 also gives the primary separation point on the symmetry line, while figure 5 shows the wall shear stress against x/D. This figure does not extend to the nose of the fin at $x/D = 0$ in order to show the details in the outer part of the interaction zone where the flow was most sensitive to the grid resolution, particularly to the value of N_η; the peaks in shear stress in the region $-1 \leqslant x/D < 0$ are much larger than those shown in figure 5 but are more robust to the value of N_η. Figure 5 shows the effect of varying the number of grid points along the symmetry line. The grids

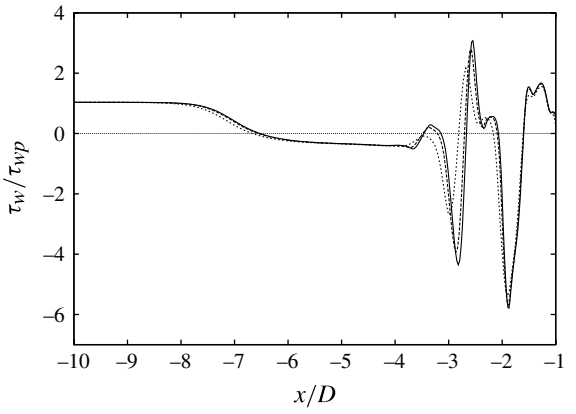

FIGURE 5. Wall shear stress ($\tau_w = \mu_w \partial u/\partial z$) on the the line of symmetry ($y = z = 0$) upstream of the $D = 7.5$ mm fin, normalized by the flat plate value $\dot{\tau}_{wp}(x)$. The grids used are: dots, G_3; dashes, G_5; solid G_6.

from G_4 onwards all show the same number of separation and attachment points (where $\tau_w = 0$), and only a small difference in τ_w between the G_5 and G_6 grids. Also, there is little difference in the primary separation point between the finer grids. The solution was most sensitive to the value of N_η, but the effects of variation in N_ζ and N_z have also been investigated. Table 2 shows little variation in the primary separation point when N_η is held constant and N_ζ and N_z varied, in particular G_3 versus G_8 and G_6 versus G_7. There was also little difference in the wall shear stress is these cases. The results presented below in §§ 4 and 5 use the grid with the largest number of grid points, i.e. the G_7 grid.

The calculations performed here have used isothermal conditions on the solid surfaces, as commonly used in investigations of this kind. Although this can be enforced numerically, the experiments rely on a temperature change at the surface in order to estimate the heat flux. It is assumed, however, that the rise in temperature does not significantly affect the flow, or the heat flux, over the duration of the run. A calculation was performed using the G_3 grid with a higher surface temperature of 309 K, the blue-start temperature of the liquid crystals. This gives a change of 4 % in the wall temperature relative to the difference between the wall temperature and the free-stream temperature T_∞ of 63 K. There was a similar, consistent, decrease in the physical values of the surface heat flux of around 6.5 %, and the wall shear stress of 2 %. However, the surface values predicted by the Eckert formulae also change by approximately 6.5 % and 2 % respectively, so that, when normalized on the flat plate values there was virtually no change in the surface heat flux and wall shear stress distributions, e.g. in τ_w as shown in figure 5. Further, there was no significant change in the flow pattern. Hence, the flow appears robust to a modest change in the wall temperature.

A uniform inflow is assumed in the calculations. This is assumed to represent the experimental conditions, but may introduce some difference between the numerical and experimental results. Similarly, the side conditions are approximate with regard to the exact experimental conditions. However, given the high speed of the flow, any errors introduced by these assumptions should be small.

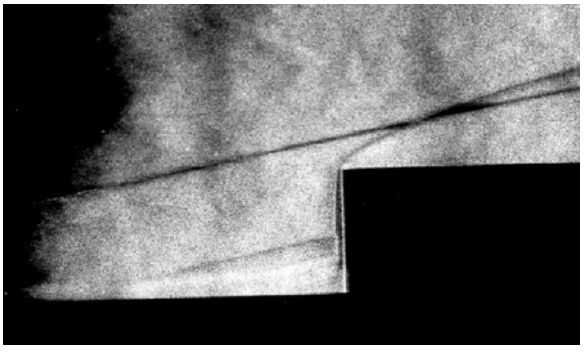

FIGURE 6. Schlieren photograph for flow past a $D = 7.5$ mm fin.

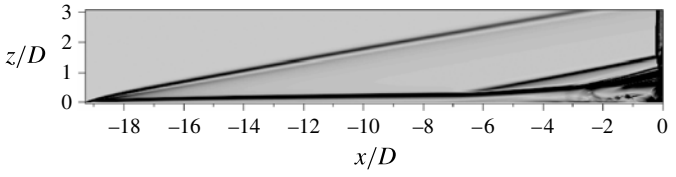

FIGURE 7. Schlieren from the numerical solution for flow past a $D = 7.5$ mm fin.

4. $D = 7.5$ mm **fin**

Experiments were performed with fins with leading-edge diameters of 2.5, 5 and 7.5 mm. In this section we consider the flow past a 7.5 mm diameter fin as the base case as this has the best spatial resolution in terms of the pixel size versus the diameter, which is the fundamental scale for the flow in the interaction region.

4.1. *Flow along the symmetry line*

First we consider the flow along the symmetry line ($y = 0$) upstream of the fin, comparing the numerical results with those available from the experiments. A standard way of visualizing high-speed flow is through schlieren photographs, which show strong density gradients, in particular the presence of shocks in supersonic flow. Figure 6 shows a schlieren image for the flow along the line of symmetry, and figure 7 a schlieren-like plot generated from numerical data by plotting $G = \alpha \exp(-\beta\,|\nabla\rho|/|\nabla\rho|_{max})$, $\alpha = 0.8$ and $\beta = 600$, on a greyscale. Schlieren photography is a 'line-of-sight' method which shows an integrated view of the density gradient variation illuminated by the light source. In contrast, the numerical schlieren plots use the gradient from the two-dimensional view of the flow in a plane, not the full, three-dimensional, flow field. As such, the numerical plots show better definition than the integrated three-dimensional view from the experimental photographs.

Figures 6 and 7 show a shock wave originating at the leading edge of the plate, but the shock in the experiments is at a larger angle to the plate. The height of the fin is 25 mm, i.e. $3.33D$. From figure 6, the leading-edge shock is at the height of the fin at $x/D \approx -4.5$ in the experiment (an angle of approximately 12.5°), whereas it is this height at $x/D \approx -2$ in the numerical solution (an angle of approximately 11°). The fact that leading-edge shock is different in strength and/or inclination in the numerical solution from that found in the experiments is not surprising or

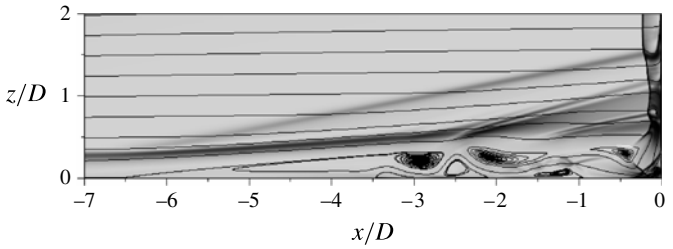

FIGURE 8. Schlieren and streamlines from the numerical solution for flow past a $D = 7.5$ mm fin.

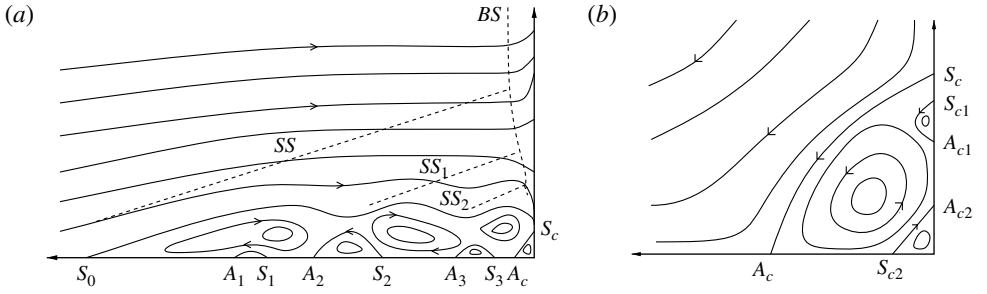

FIGURE 9. Schematic of the flow, (*a*) on the centreline upstream of the fin in the interaction region and (*b*) in the corner. Solid lines are streamlines and dashed lines represent shocks. The shocks are the bow shock (*BS*), the separation shock (*SS*) and secondary shocks (SS_1 and SS_2). The primary separation point is labelled S_0, while S_1–S_3 are separation points on the plate and A_1–A_3 the corresponding attachment points. S_c and A_c denote the separation and attachment points for the primary corner vortex, and S_{c1}, S_{c2}, A_{c1} and A_{c2} separation and attachment points for the secondary corner vortices embedded within the primary corner vortex.

meaningful. Theoretically, for an inviscid flow past an infinitely thin plate perfectly aligned with the flow, there would be no leading-edge shock. In the experiments, the shock arises from two causes: the finite though small radius of curvature at the leading edge, and the viscous interaction at the leading edge. The strength and angle of the leading-edge shock depends on how close the actual situation is to the ideal case. The minimum possible angle for a disturbance originating at the leading edge, is that of a Mach wave, given by $\sin^{-1}(1/M_\infty) = 8.4°$, which would reach the fin at a height of $2.85D$, impacting on the fin, rather than passing above it. In contrast, in the numerical simulations, the shock arises only from the viscous interaction, as an infinitely thin leading edge can be modelled, and the difference in the numerical and experimental results for the leading-edge shock shows primarily that the numerical setup approximates the ideal situation more closely than in the experiments. In either case, the leading-edge shock is weak, and will have little effect on the flow in the vicinity of the fin–body junction. Numerically there is a 6 m s^{-1} change in the free-stream velocity (0.5 %) at a height $2D$ above the plate as the flow passes through the leading-edge shock.

As expected, more detail of the flow can be seen in the numerical solutions than appears in the schlieren image from the experiments, particularly in the boundary layer and in the corner at the fin–plate junction. Figure 8 shows a schlieren-type plot and

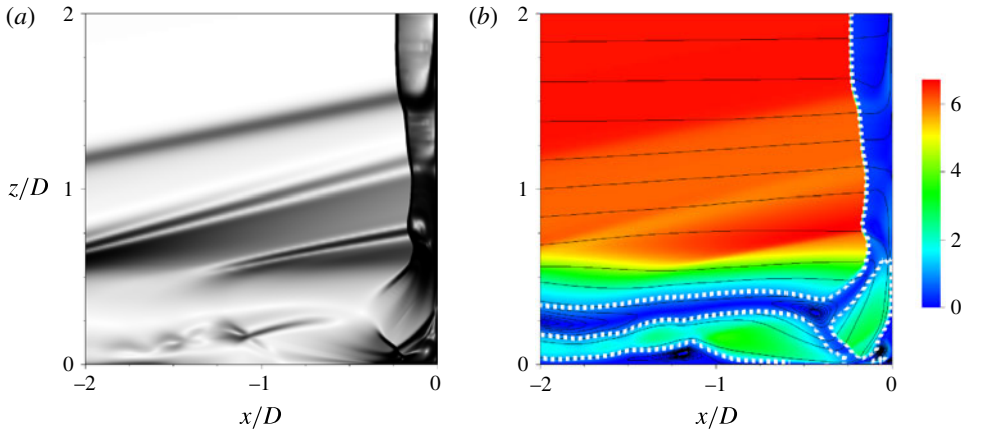

FIGURE 10. (Colour online) (*a*) Numerical schlieren and (*b*) Mach number, streamlines (solid lines) and sonic line (dashed) for the corner flow on the symmetry line upstream of the fin.

streamlines for the flow near the wall along the symmetry line in the separation region, while figure 9 shows a schematic of the flow on the centreline based on the numerical and experimental results. The streamline pattern shown here is similar to that inferred from experimental measurements of surface quantities by e.g. Hung & Clauss (1981).

All of figures 6–8 show the primary separation shock (labelled *SS* in figure 9), and the bow shock, with a significantly larger stand-off distance for the bow shock above the shock–shock interaction point. The difference in the stand-off distance reflects the fact that, since the density above the shock–shock interaction point is lower than that below the interaction, a larger stand-off distance is necessary for the bow shock to pass the required mass flow rate. From figure 6, the location of the shock–shock interaction, where the separation shock impinges on the bow shock, occurs at $z \approx 1.5D$, which agrees well with that found in the numerical solution (figure 7). Further, both the experimental and numerical results have the separation shock at approximately 11° to the plate. This indicates good agreement in the interaction process upstream of the fin. The schlieren-type plots shown in figures 8 and 10 also show that in addition to the primary separation shock, there are two secondary shocks (labelled SS_1 and SS_2 in figure 9) corresponding to changes in slope of the streamlines with an expansion fan between them.

Figure 10 shows the numerical schlieren and the Mach number with streamlines and sonic line ($M = 1$) in the corner, and figure 11 the normalized wall shear stress near the corner (the wall shear stress upstream of the corner in the interaction region is shown above in figure 5).

The streamlines (figure 8) and wall shear stress (figures 5 and 11) show that embedded within the separation, which rotates clockwise as viewed in figure 8, there are primary vortex cores, with a relatively strong clockwise rotation, and a number of smaller secondary eddies, rotating counterclockwise, on the wall adjacent to the primary cores. There is a complex shock and expansion structure in the corner region (figure 10), which corresponds to rapid changes in the speed and direction of the flow, with supersonic regions in the boundary layer bounded above and below by subsonic regions. The streamlines (figures 9 and 10*b*) show an eddy/recirculation region in the corner, with counterclockwise rotation. However, as shown by the wall

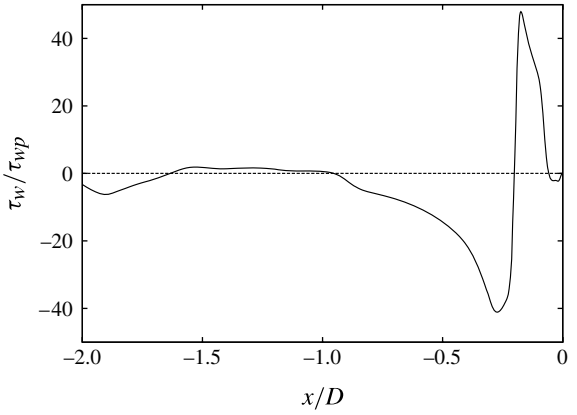

FIGURE 11. Wall shear stress normalized on the flat plate values on the the line of symmetry ($y = z = 0$) upstream of the $D = 7.5$ mm fin.

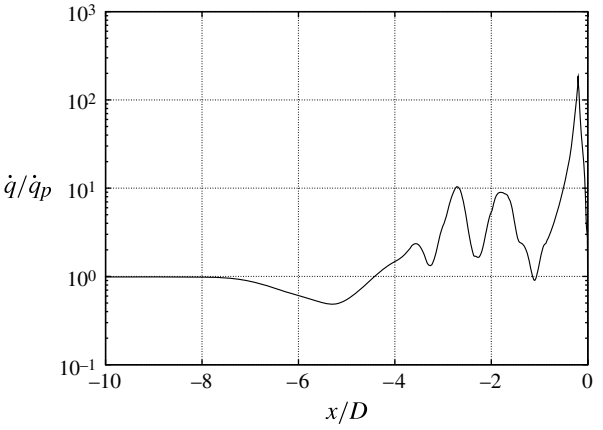

FIGURE 12. Heat transfer rate on the the line of symmetry ($y = z = 0$) upstream of the $D = 7.5$ mm fin, normalized by the flat plate value.

shear stress (figure 11) there is also smaller recirculation with clockwise rotation in the corner, underneath the main corner vortex. The largest wall shear stress values are found either side of the attachment at the outer edge of the main corner vortex, at $x/D \approx -0.2$ (feature A_c in figure 9), with a corresponding rapid change in Mach number close to the wall.

The peak heating rate on the surface of the plate also occurs in this region. Figure 12 shows the heat transfer rate ($\dot{q}$) normalized by the flat plate value ($\dot{q}_p(x)$) along the symmetry line ahead of the fin (shown on a log scale for clarity). As expected for laminar interactions, there is a drop in the heat transfer rate as the flow goes through separation, followed by a region of enhanced heating where the interaction induced by the presence of the fin is strongest. The largest peak in $\dot{q}$, with $\dot{q}/\dot{q}_p \approx 180$, occurs at the attachment point for the major corner eddy ($x/D \approx -0.2$; A_c in figure 9). The other three peaks in $\dot{q}$ (at $x/D \approx -1.7$, -2.7 and -3.6) occur downstream (locally) of the attachment points of the wall eddies (A_1–A_3 in figure 9).

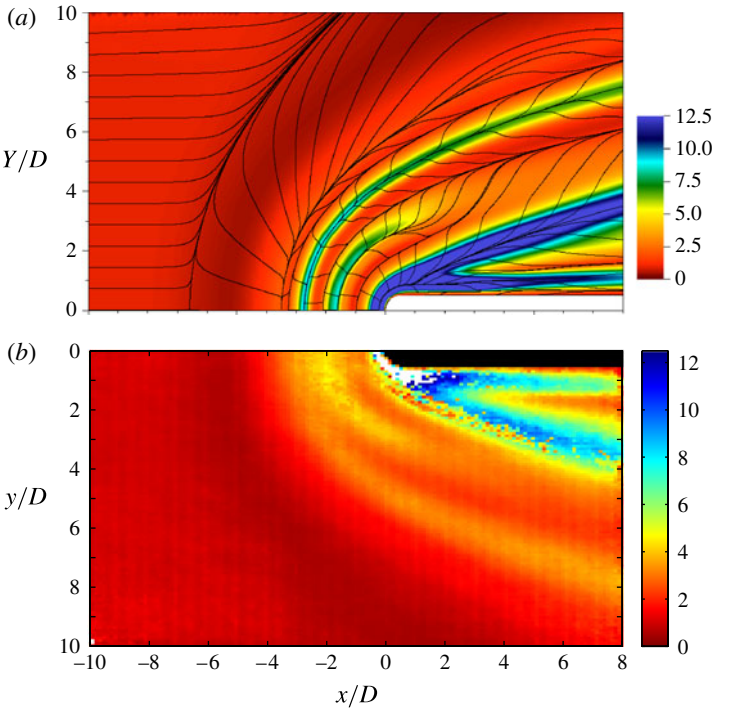

FIGURE 13. (Colour online) Heat transfer rate on the plate for the $D = 7.5$ mm fin, normalized on flat plate values: (*a*) numerical; (*b*) experimental.

The troughs in $\dot{q}$ between these peaks occur in the regions occupied by the secondary wall eddies. Upstream of the interaction zone, $\dot{q}$ closely matches the values predicted from the Eckert correlation ($\dot{q}_p(x)$), as expected.

4.2. *Plate surface values*

The experiments with liquid-crystal thermography (§ 2.3 above) provided quantitative estimates of the heat flux distribution on the surface of the plate. Figure 13 shows the heat flux on the plate, normalized on values for a flat plate ($\dot{q}_p(x)$) so that it shows the effect of the fin on the heat flux values. Note that in this and similar figures shown below the maximum value used on the scale for the heat flux presented for the numerical results is $\dot{q}/\dot{q}_p = 12.5$ in order to provide a sensible comparison with the experimental results. In reality, the peak heating rates are higher in the numerical solution (see figure 12).

There is a good match between the pattern shown in the experiments and that obtained numerically. The features in the numerical results are more clearly defined. In particular, several of the peaks of heat transfer on the symmetry line identified in the numerical values (figure 12), are smeared in the experimental results, whereas away from the symmetry line, these peaks are clearly separate in both the numerical and experimental results. The smearing arises from the limitations of the experimental technique, in particular, underestimation of the heat fluxes by the liquid crystals in regions where the heating is very high, coupled with cross-conduction effects and the relatively low resolution, as discussed in § 2.4.

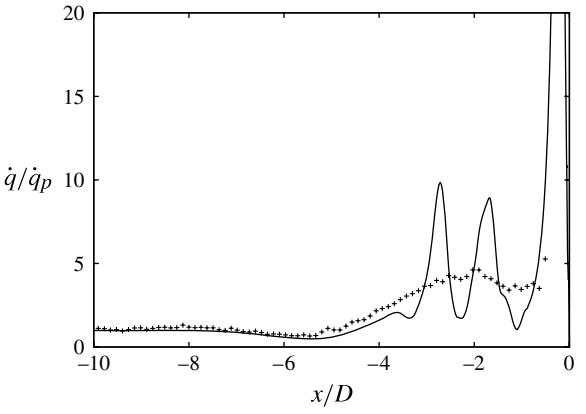

FIGURE 14. Symmetry line surface heat transfer rate upstream of the fin normalized on flat plate value for the $D = 7.5$ mm fin: solid line, numerical solution; symbols, experimental values.

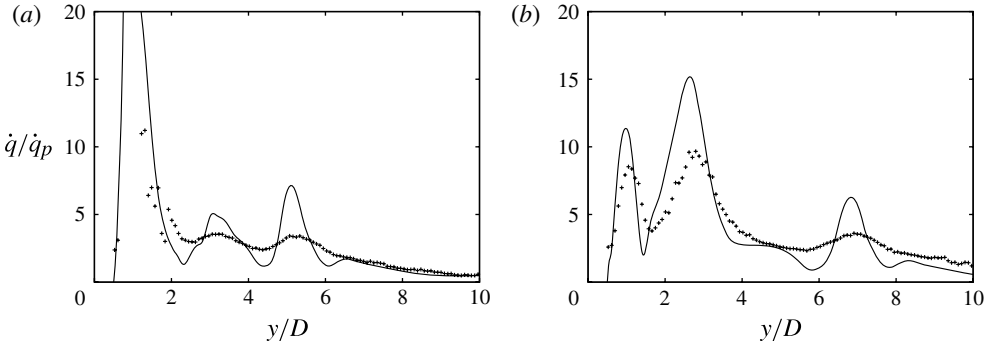

FIGURE 15. Cross-flow surface heat transfer rate normalized by the flat plate value for the $D = 7.5$ mm fin. Solid line, numerical solution; symbols, experimental values. (*a*) $x/D = 1$; (*b*) $x/D = 5$.

Starting from the fin and going outwards, the first major region of elevated heat transfer shown in the downstream region of figure 13 is associated with the attachment of the flow in the corner vortex (originating at A_c on the symmetry line in figure 9). The next region of elevated heating is associated with the interaction of the bow shock and the boundary layer, causing attachment of the lateral flow in the cross-plane. This is discussed further when the off-surface flow is considered (§ 4.3 below). Another band of elevated heating, originating at attachment point A_3 on the symmetry line, weakens and eventually vanishes as the flow proceeds round the nose of the fin. Further outboard there is another peak due to the attachment originating at A_2 in figure 9. A low-amplitude peak is found still further out, originating from the attachment of another secondary wall vortex at A_1 on the symmetry line. The dip in heat transfer in the region with the primary separation can be seen in both set of results (the darker colour where $\dot{q}/\dot{q}_p < 1$).

Figure 14 shows a comparison of the experimental and numerical surface heat transfer rates along the symmetry line upstream of the fin, and figure 15 the

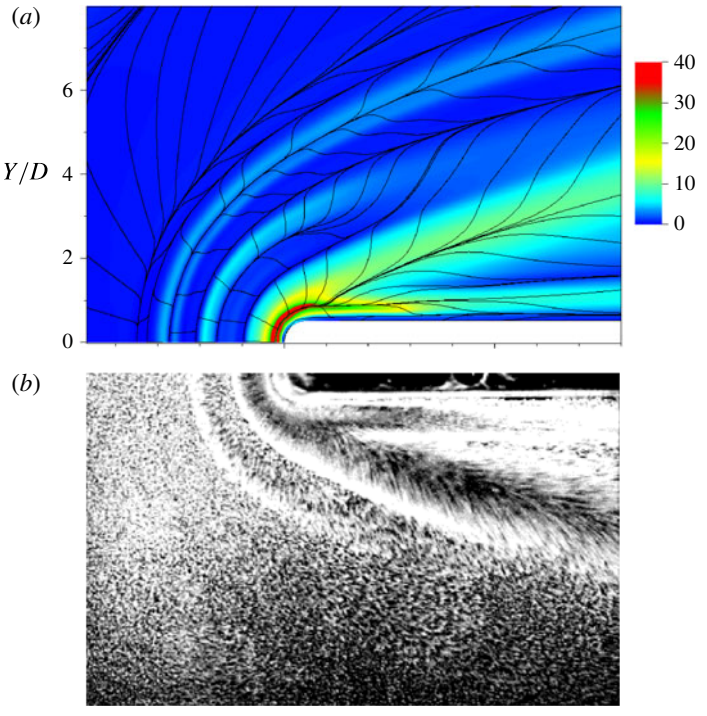

FIGURE 16. (Colour online) Flow pattern on the plate for the $D = 7.5$ mm fin. (*a*) Numerical, surface streamlines with the wall shear stress magnitude normalized on the flat plate value at the nose of the fin. (*b*) Experimental, surface oil flow.

corresponding plots normal to the fin at $x/D = 1$ and $x/D = 5$. Again these are normalized by flat plate values. Ahead of the fin (figure 14), upstream of the interaction region both the experimental and numerical values are in good agreement and close to that of the undisturbed laminar flow, as expected. Both the experimental and numerical heat fluxes reduce as the boundary layer thickens and then separates (at $x/D \approx -6.5$) due to the fin–plate interaction. The separation distance is shorter than that found by Hung & Clauss (1981) (9*D*–12*D*) for Mach 5.3 laminar cylinder–plate flow, but the numerical and experimental data are in good agreement in this region. Further inboard the heat flux increases but the lack of resolution and range in the liquid-crystal response, noted earlier, is evident from the absence of the peaks displayed in the numerical results. In the transverse direction (figure 15), the experimental results show evidence of localized heating, but again, the magnitudes of the peaks are underestimated compared with the numerical values. However, the locations of the peaks are in quite close agreement. There are gaps in the experimental data near the nose of the fin (shown as white in figure 13*b*) where the heat flux was too high to provide valid data.

In addition to heat transfer measurements, experiments were performed using a surface oil flow technique to visualize the shear stress distribution on the surface of the plate. Figure 16(*b*) shows a photograph of the distribution of the oil at the end of an experiment, and surface streamlines and the magnitude of the wall shear stress from the numerical solution (figure 16*a*). The numerical plot shows much more detail of the flow due to the lack of movement of the oil in the experiments in low-shear regions.

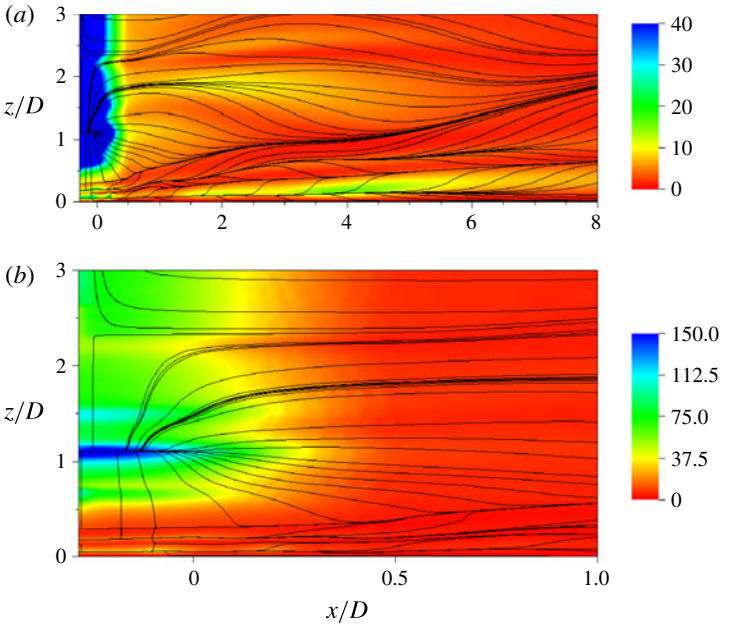

FIGURE 17. (Colour online) Surface heat transfer rate and surface streamlines, (*a*) on the 7.5 mm fin and (*b*) for the nose region, normalized by the flat plate value at the nose of the fin. The *x*-scale is the non-dimensional distance along the surface from the downstream end of the nose with the origin placed so that $x/D = 0.5$ there, with the nose of the fin at $x/D = \pi/4 - 1/2$ rather than 0 in this figure.

However, there is generally good agreement between the numerical and experimental results. In particular, the white regions in the experimental photograph correspond to regions of low shear stress, adjacent to regions of relatively high shear stress, where the oil naturally accumulates. Regions with little oil are regions of very high shear stress, but there are also regions with elevated shear stress where there is no visible effect on the distribution of oil. The areas with high shear stress, particularly near the nose of the fin, match the regions with high heat transfer rates as shown in figure 13.

4.3. *Off-surface flow*

Apart from the schlieren photograph of the symmetry line flow upstream of the fin (figure 6), the experimental facility did not allow off-surface measurements or visualizations of the flow. However, the good overall agreement between the numerical and experimental results for the plate surface enable us to investigate the off-surface behaviour of the flow from the numerical solution with confidence. Figure 17 shows the heat transfer rate on the surface of the fin and the surface streamlines of the flow. The heat transfer rate is normalized using the flat plate value at the origin ($\dot{q}_{ref} = \dot{q}_p(0)$), i.e. at the nose of the fin. In general, the heating rates are higher on the fin than on the plate, so scales with a wider range of values are used to visualize the heat flux distribution for the fin than used above for the plate. As expected, there are very high heating rates on the nose of the fin, particularly in the regions of shock–shock interactions ($z/D \approx 1$ and 1.5). The maximum value for the surface heat flux in the fin–body interaction zone is found on the nose of the fin in the region where the secondary shock (SS_1 in figure 9) meets the bow shock ($z/D \approx 1$),

where $\dot{q}/\dot{q}_{ref} \approx 175$. In comparison, the peak value of $\dot{q}/\dot{q}_{ref}$ in the region where the separation shock (*SS* in figure 9) meets the bow shock is around 115. An alternative value which could be used to normalize the heat flux in the nose region is $\dot{q}_f$, the heat flux for a fin normal to the free stream above the interaction zone, which was found to be 2×10^5 W m^{-2} for the 7.5 mm fin, consistent with predictions from previous work (§ 3). This value is approximately 80 times $\dot{q}_f$, illustrating the extremely high heating that would be found on a fin regardless of any fin–body interaction effects. In these terms, the peak heat flux found on the stagnation line is approximately double that for undisturbed flow past a fin, i.e. approximately $160\dot{q}_{ref}$. In comparison, the highest value of $\dot{q}/\dot{q}_{ref}$ on the surface of the plate is on the symmetry line just upstream of the nose at the attachment point of the corner vortex (A_c in figure 9), with a value of approximately 180, higher than that found on the fin. There is considerable variation in the heat transfer rates reported in the literature for configurations of this type. However, extremely high rates have been reported. For example, Hung & Clauss (1981) report a 100-fold increase over the plate value for flow on a plate ahead of a cylinder at Mach 5.3.

There is a distinct attachment line on the nose of the fin, extending downstream of the point of maximum heat flux just above $z/D = 1$. However, this attachment line, and the associated elevated level of heating, weakens rapidly downstream. Its disappearance is simply the result of the natural change in orientation of the flow relative to the fin as the flow proceeds around the nose of the fin; on the nose the incoming flow is normal to the surface but it becomes increasingly aligned along the surface as the fluid travels around the nose onto the side of the fin.

The cross-stream flow for $x/D = 1$ is shown in figure 18 and that for $x/D = 5$ in figure 19. These figures give numerical schlierens and pseudo-streamlines generated using the cross-stream velocity (i.e. $(0, v, w)$), and contours of the velocity magnitude for the cross-stream flow. On the right of the schlierens near the lateral edge of the plate, there are two pronounced dark regions, corresponding to the edge of the boundary layer (lower) and the primary separation shock (upper). Also clearly shown are shocks and expansion fans which are the lateral extensions of these features seen in the symmetry line flow upstream of the fin (figures 8–10).

Figures 18 and 19 also show the development of the corner vortex at the fin–plate junction, which grows significantly in size between $x/D = 1$, and $x/D = 5$. The flow is down the wall on the fin, with the main vortex rotating clockwise when viewed from downstream. The structure of the flow in the corner is essentially that shown on figure 9(*a*) (with a different apparent rotation to the vortex due to the different orientation of the view). In fact, the corner vortex along the fin is the continuation of that found in the corner on the symmetry line (S_c and A_c in figure 9), with similar features. At $x/D = 5$, the primary separation on the fin for the corner vortex occurs at $z/D \approx 1$, which can be matched with the separation line shown in the same position in figure 17. The downstream development of the corner vortex can be seen by tracking this separation line along the fin from the nose (S_c in figure 9). Similarly, the attachment line of the corner vortex can be tracked along the surface of the plate (it lies within the region of high heat transfer closest to the fin, shown as dark/blue in figure 13, with $y/D \approx 1$ at $x/D = 5$) from the centreline (A_c in figure 9).

There are also two small, counter-rotating, secondary vortices embedded within the main corner vortex. One sits under the main vortex in the corner (again the downstream continuation of the small vortex found in the symmetry line flow; S_{c2} and A_{c2} in figure 9). Its development can be tracked from the separation and attachment lines closest to the fin in figure 13 (the attachment line closest to the fin) and figure 17

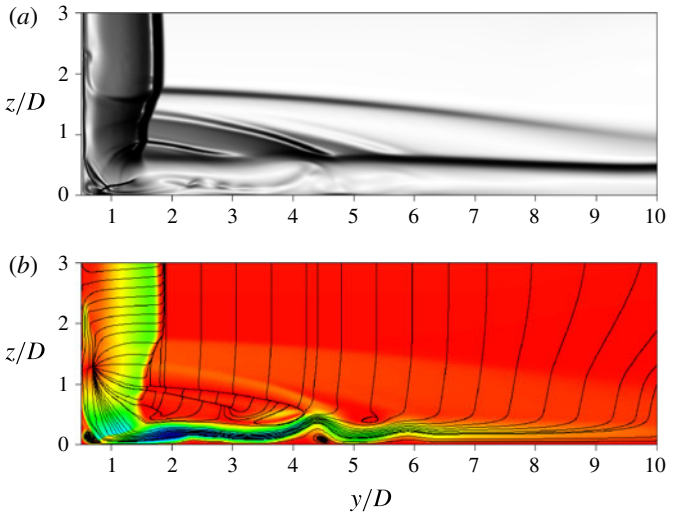

FIGURE 18. (Colour online) Cross-stream flow patterns looking upstream for the $D = 7.5$ mm fin at $x/D = 1$. (*a*) Numerical schlieren ($\beta = 100$, $|\nabla\rho|_{max} = 50.4$). (*b*) Pseudo-streamlines using the cross-stream velocity (v, w), and the cross-stream velocity magnitude (dark/red 0 m s^{-1}, light/blue 900 m s^{-1}).

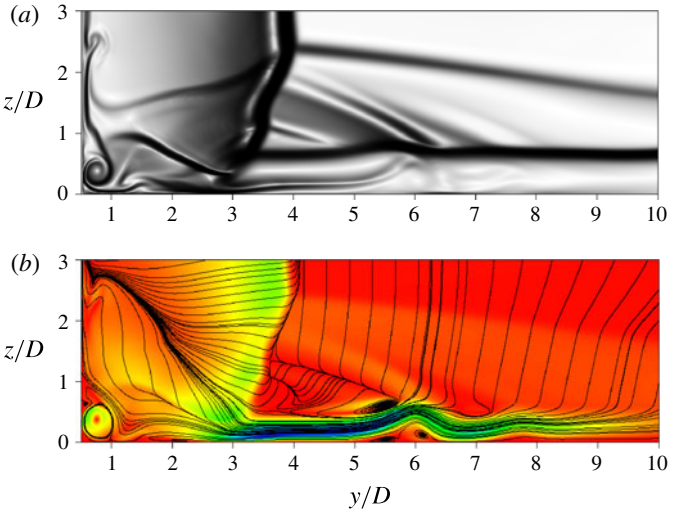

FIGURE 19. (Colour online) Cross-stream flow patterns looking upstream for the $D = 7.5$ mm fin at $x/D = 5$. (*a*) Numerical schlieren ($\beta = 20$, $|\nabla\rho|_{max} = 5.3$). (*b*) Pseudo-streamlines using the cross-stream velocity (v, w), and the cross-stream velocity magnitude (dark (red) 0 m s^{-1}, light (blue) 700 m s^{-1}). The streamlines near the wall are down the wall, with the corner vortex rotating clockwise.

(the lowest separation line). The other secondary vortex is attached to the fin on the upper side of the main corner vortex (around $z/D = 0.7$ in figure 19). Its separation and attachment lines can be seen in figure 17 (at $z/D \approx 0.8$ and $z/D \approx 0.5$ at $x/D = 5$ respectively), lying between the separation line for the main vortex and the attachment

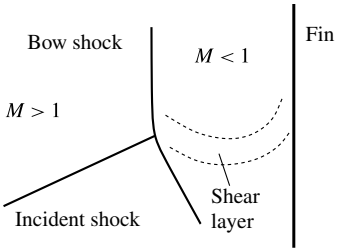

FIGURE 20. Schematic for shock–shock interaction along the symmetry line ahead of the fin. The region between the bow shock and the fin is completely subsonic.

line for the secondary corner vortex. Again, it can be tracked back to the nose of the fin (between S_{c1} and A_{c1} in figure 9). The region of high heat flux extending along the fin above the plate shown in figure 17 lies above the attachment line for the secondary vortex in the corner, and below the separation line for the secondary vortex on the fin, underneath the main corner vortex. Small secondary vortices of the type seen here are generated by viscous forces, and are commonly found in laminar corner flows, including incompressible flow, e.g. in cavity flow (Shankar & Deshpande 2000).

There is a strong interaction between the separation shocks and the bow shock, changing the alignment of the bow shock with the fin. Figure 20 shows a schematic diagram of the interaction between the primary separation shock and the bow shock, based on the numerical solution along the symmetry line ahead of the fin. A shear layer, with the flow as viewed in figure 20 rotating anti-clockwise, is generated at the interaction by the action of the shocks, which both change the magnitude of the velocity and redirect the flow as it passes through the shocks in this region. Note that Crocco's theorem (see e.g. Anderson 1990) implies that vorticity must be generated in this region as the bow shock in the region of the triple point is curved not rectilinear. There are distinct peaks in the Mach number and velocity of the flow along the lower edge of the shear layer, giving the appearance of a subsonic jet in this region, but, since the vorticity is single-signed, we regard this feature of the flow as primarily a shear layer rather than a jet. In the region of the interaction, the flow between the bow shock and the surface of the fin along the symmetry line is entirely subsonic. Interactions between bow and incident shocks are commonly discussed with reference to the classification scheme introduced by Edney (1968), who performed experiments with an incident shock generated by a wedge impinging on a bow shock generated by a hemisphere at Mach numbers of 4.6 and 7. The shock structure in figure 20 is closest to a type III Edney interaction. However, a type III interaction has a shear layer between subsonic and supersonic regions, whereas here, the flow is subsonic on both sides of the shear layer. The flow as sketched in figure 20 is similar to that postulated by Hiers & Loubsky (1967) from their experiments on a laminar Mach 14 flow past a fin with a Reynolds number of $Re_D = 8 \times 10^3$, based on the free-stream values and fin diameter (cf. $Re_D = 3.8 \times 10^4$ for the 7.5 mm fin in the current work). Hiers & Loubsky (1967) predicted that a vortex sheet would be generated at the shock–shock intersection. The shear layer found here is a finite-Reynolds number-manifestation of this vortex sheet, but is curved rather than straight, with a drop in pressure across the layer (see e.g. Anderson 1990 for a discussion of shock–shock intersections in general).

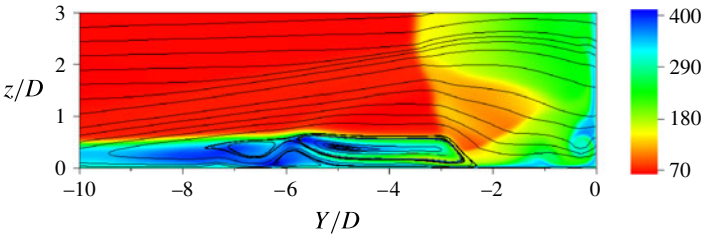

FIGURE 21. (Colour online) Cross-stream flow patterns for the $D = 7.5$ mm fin at an angle to the flow: $(6, 0.5)D$ to $(2.4, 10)D$. Y is the distance along the line, not normal to the fin. The map shows the gas temperature (K).

Examination of the numerical solution shows that the effect of the shear layer impinging on the surface of the fin on the symmetry line is felt a significant distance above the interaction point. The extent of the shear layer's influence can be seen in figure 17, from the interaction point at $z/D \approx 1.5$ to the upper limit at the band of lower heat transfer at $z/D \approx 2.3$.

Flow similar to that shown in figure 20 is also found at the interaction of the two secondary shocks (labelled SS_1 and SS_2 in figure 9) and the bow shock. Further, as mentioned above, a calculation was performed with a fin 45 mm high ($z/D = 6$ with $D = 7.5$ mm) in order to check the influence of the position of the upper boundary. This fin was high enough for the leading-edge shock to meet the bow shock within the computational domain, at $z/D \approx 3.5$. Again, the flow pattern shown in figure 20 was found in the vicinity of this shock–shock interaction.

As the flow proceeds around the nose from the shock–shock interactions, the velocity increases until there is supersonic flow between the bow shock and the fin. Supersonic flow first occurs at approximately 30° around the nose from the symmetry line, in the region of the interaction point of the separation shock and the bow shock, and increases in extent until, by approximately 60° from the nose, the flow is completely supersonic apart from in the boundary layer at the fin wall (and in the region at the fin–plate junction where the flow is directly influenced by the boundary layer on the plate). However, the shear layer generated at the shock–shock interaction point persists around the nose and along the fin wall. It can be seen clearly in the numerical schlieren plot in figure 19(*a*) for $x/D = 5$, extending from the bow shock. The hairpin-like structure at the wall is part of this interaction, originating from $z/D \approx 2.3$ at the nose, the area highest on the nose of the fin where the shear layer (figure 20) has a direct effect.

While data plotted on a plane normal to the fin give a good indication of the nature of the flow between the bow shock and the wall, and above the separation shock, they do not reveal the details of the flow in the boundary layer on the plate away from the fin. In particular, there is little evidence in the cross-flow streamlines shown in figures 18 and 19 of the vortical structure implied by the surface streamlines on the plate shown in figures 13 and 16. This is because the flow outside the bow shock in the interaction region does not run parallel to the fin, but at an angle to it, as shown by the surface streamlines in figure 13. Figure 21 shows pseudo-streamlines for flow in a plane from $(x, y) = (6, 0.5)D$ to $(2.4, 10)D$, a line approximately perpendicular to the main direction of flow near the surface, using the velocity tangential to this plane and normal to the plate (w). This figure is presented with the distance measured away from the fin in a negative sense (Y) so that it can be compared directly with the figure for

the symmetry line flow upstream of the fin (figure 8). Also shown is the temperature of the gas. A schlieren-type plot is not shown as it similar to that in figure 19.

The vortical structure of the flow can now be seen clearly. Away from the fin, there is a continuation of the flow along the symmetry line ahead of the fin shown in figure 8, and two main cores of the vortex and two small secondary wall vortices shown in figure 21 can be tracked downstream from those shown in figure 8, and in figure 9 as the two cores furthest upstream and the wall vortices sitting between A_1 and S_1 and A_2 and S_2. However, the other wall vortex seen in figure 8 (between A_3 and S_3 in figure 9) no longer exists. Its disappearance coincides with that of the region of elevated surface heat transfer seen in figure 13 (at $x/D \approx 0.5$ and $y/D \approx 3$). Inspection of the solution shows that as the flow proceeds around the nose of the fin, the bow shock moves away from the wall of the fin, and that its interaction with the boundary layer generates a strong flow towards the surface of the plate, leading to an attachment on the plate surface, as shown in figure 21, at $Y/D \approx -2.4$.

As viewed from this perspective, the attachment generated by the bow shock–boundary layer interaction marks the boundary on the surface between the outer vortical flow originating along the symmetry line ahead of the fin, and the inner flow which is largely aligned with the fin. This attachment line can be seen in figure 13 as the outer band of high heat transfer shown as blue. As seen in figure 21 there is a relatively strong flow along the surface of the plate outwards from this attachment, and as the flow proceeds around the nose of the fin this is sufficiently strong to overcome the vortical motion in the wall vortex originating between A_3 and S_3 on the centreline (figure 9), leading to its destruction, along with the associated band of high heating.

By tracking the development of the flow from the symmetry line, the ridges of high surface heat transfer seen on the plate in both the experimental and numerical results (figure 13) can now be clearly associated with major flow features. Along the side of the fin, the band of high heat transfer closest to fin (dark/blue in figure 13) lies along the attachment line for the main corner vortex. The second band of high heat transfer (also dark/blue in the figure), marks the attachment line arising from the bow shock–boundary layer interaction. Near the nose, these regions coincide, with only a single band of high heat transfer, matching the peak closest the fin in figure 12. The outer band of high heat transfer downstream on the plate (dark/green in figure 13) marks the attachment (A_2 in figure 9) of the secondary vortex on the plate seen in all of the figures showing cross-stream flow (figures 8 and 18–21).

5. Variation of fin size

In order to investigate scaling effects, experiments were also conducted with fins with $D = 2.5$ mm and 5 mm. Matching numerical simulations have been performed. Figures 22–24 show in turn the normalized numerical and experimental surface heat transfer rates for the $D = 2.5$ mm fin for the plate, along the symmetry line upstream of the fin, and normal to the fin at $x/D = 1$ and $x/D = 5$. Note that the spatial resolution of the experimental data with $D = 2.5$ and 5 mm has been degraded relative to the fin diameter due to the fixed pixel size. This can be seen clearly in figures 23 and 24 where the experimental data are plotted at the resolution of the pixels. However, there is still good agreement between the experimental and numerical results with respect to the positions of the peaks and troughs in the heat transfer rate transverse to the fin (figure 22), but there are large gaps in the experimental data reflecting the fact that, in the peak regions, the change in surface temperature was too fast to allow an estimate of $\dot{q}$ to be made. On the symmetry line (figure 23) the

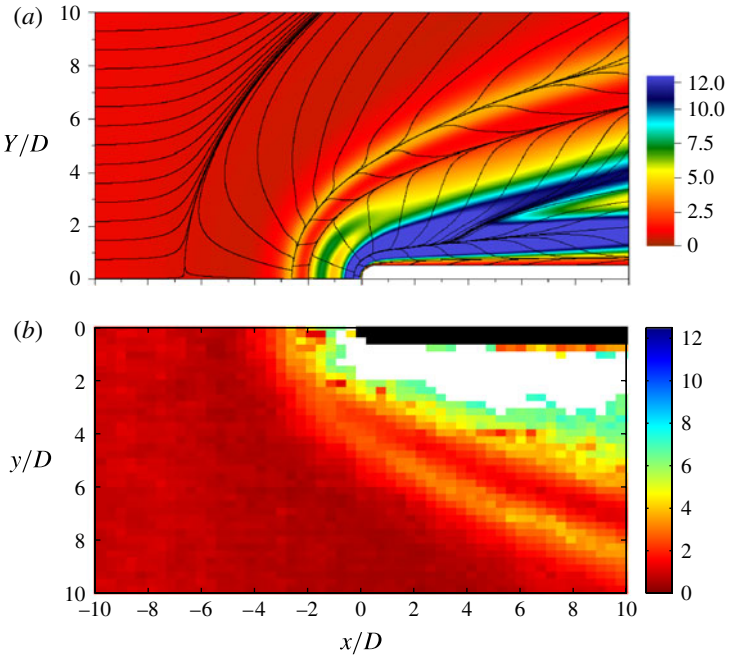

FIGURE 22. (Colour online) Heat transfer rate on the plate for the $D = 2.5$ mm fin, normalized on flat plate values: (*a*) numerical; (*b*) experimental. The white shows areas in the experimental results where it was not possible to obtain an estimate of the heat transfer rate.

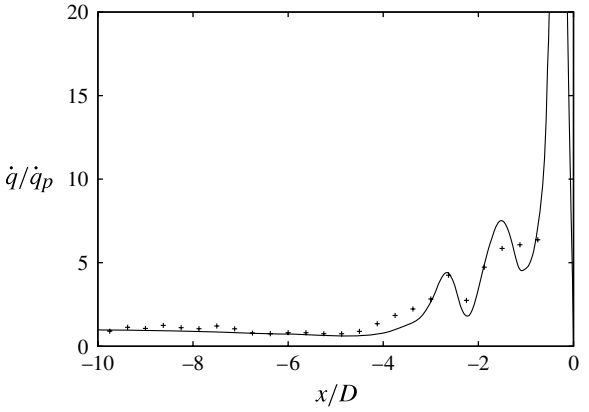

FIGURE 23. Symmetry line surface heat transfer rate upstream of the fin normalized by the flat plate value for the $D = 2.5$ mm fin. Solid line, numerical solution; symbols, experimental values.

comparison is again limited by the resolution and range of the experimental results. These figures are similar to those above for the 7.5 mm fin (figures 13–15) reflecting the fact that in the fin–body interaction zone the flow scales primarily with the fin diameter.

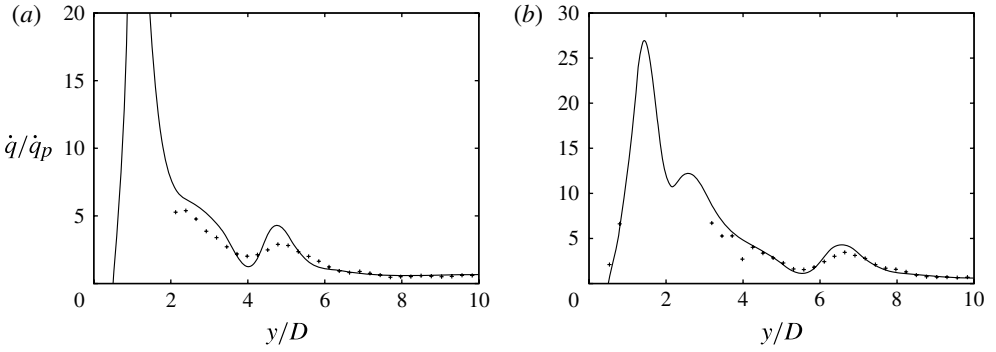

FIGURE 24. Cross-flow surface heat transfer rate normalized by the flat plate value for the $D = 2.5$ mm fin. Solid line, numerical solution; symbols, experimental values. (*a*) $x/D = 1$; (*b*) $x/D = 5$.

Figures 25–27 show in turn the normalized numerical and experimental surface heat transfer rates for the $D = 5$ mm fin for the plate, along the symmetry line upstream of the fin, and normal to the fin at $x/D = 1$ and $x/D = 5$. Again, there is agreement in the overall pattern of the heat transfer, but there is also a noticeable lateral displacement of the region of elevated heat transfer (the outer band shown as light/yellow in figure 25 and the peak to the right in figure 27) and the associated attachment line, with this feature closer to the fin in the experiments than in the simulations.

Figure 28 shows a comparison of the heat transfer rates between the different diameter fins for both the experimental and numerical values at $x/D = 5$. From this it is clear that it is the experimental values for $D = 5$ mm that are anomalous with respect to the mismatch in position for the outermost peak: in the simulations, the position of this peak in terms of y/D is approximately the same for all three fins, while, in comparison, the position of the peak in the experimental results is significantly displaced towards the fin for the 5 mm fin, in comparison with the other two cases. Note that some variation between the positions of the flow features would be expected even in perfect conditions, since the thickness of the boundary layer relative to the diameter should also play a role, and this is different in each case. However, the agreement between the 2.5 and 7.5 mm fins, but not the 5 mm suggests other factors are responsible for this particular variation. That there is some variation in the experimental results is not surprising. Unlike in the simulations, where the inflow conditions can be specified exactly, there will be some variation of the experimental conditions between runs; for example, around 5 % in the stagnation values (P_0 and T_0) in the experiments. Also, in the simulations, this feature of the flow was the most sensitive to the grid resolution (in particular to the value of N_η). This reflects the fact that vortical features of this kind are sensitive to the fine details of the flow in general.

As can be seen in the various figures presented above, the flow in the outer part of the interaction zone (from the bow shock outwards) scales largely on the diameter of the fin D. However, on this scale, in the numerical values for the heat transfer rate at $x/D = 5$ shown in figure 28, the innermost peak, arising at the attachment point of the corner vortex, moves closer to the fin and its magnitude decreases as the diameter is increased. This occurs because the flow in the inner region adjacent to the wall is aligned with the wall of the fin rather than the bow shock, as can be seen from the

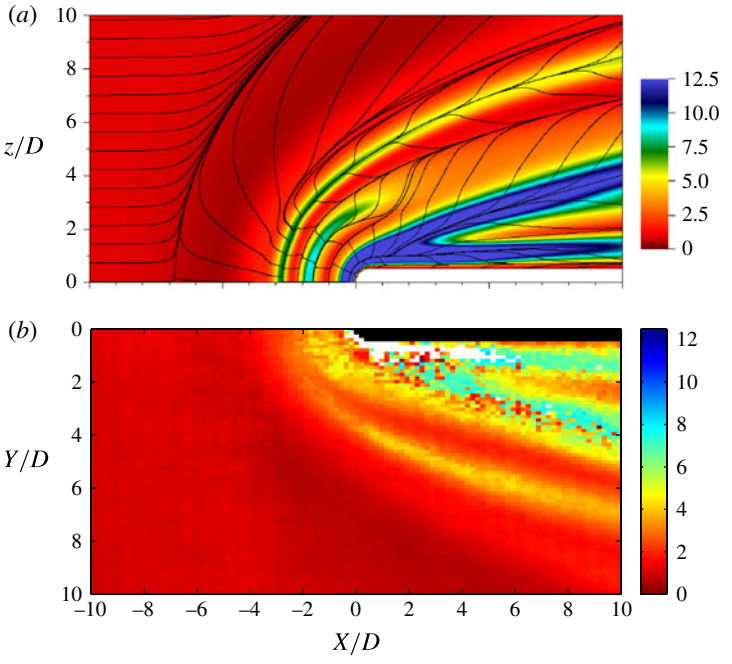

FIGURE 25. (Colour online) Heat transfer rate on the plate for the $D = 5$ mm fin, normalized on flat plate values: (*a*) numerical; (*b*) experimental. The white shows areas in the experimental results where it was not possible to obtain an estimate of the heat transfer rate.

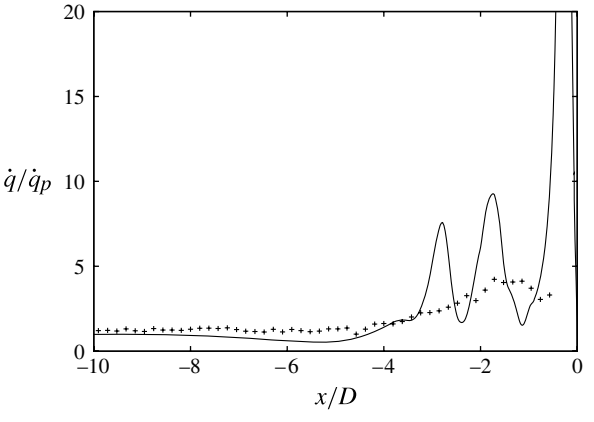

FIGURE 26. Symmetry line surface heat transfer rate upstream of the fin normalized by the flat plate value for the $D = 5$ mm fin. Solid line, numerical solution; symbols, experimental values.

surface streamlines in figures 13, 25 and 22, and varies with the distance along the wall of the fin rather than with the distance normalized by the fin diameter. This is illustrated in figure 29, which shows the dimensional heat transfer rate against distance in mm, 37.5 mm downstream from the end of the nose ($x = D/2$), for the three

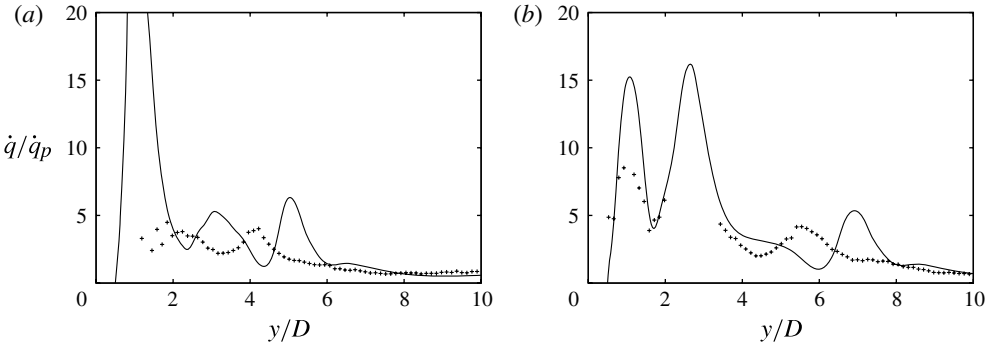

FIGURE 27. Cross flow surface heat transfer rate normalized by the flat plate value for the $D = 5$ mm fin. Solid line, numerical solution; symbols, experimental values. (*a*) $x/D = 1$; (*b*) $x/D = 5$.

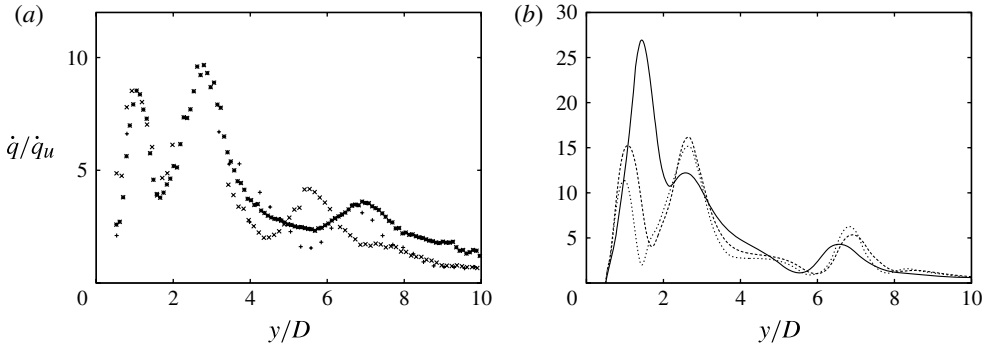

FIGURE 28. Cross-flow normalized surface heat transfer rate normalized by the flat plate value for different diameter fins for $x/D = 5$. (*a*) Experimental values (+, $D = 2.5$ mm; ×, $D = 5$ mm; ✳, $D = 7.5$ mm). (*b*) Numerical values (solid line $D = 2.5$ mm, dashes $D = 5$ mm, dots $D = 7.5$ mm).

diameters. In these dimensional terms, the innermost peaks occur at the same location for all three fins, and the magnitudes of the peaks are similar. This is the case all the way along the fin downstream of the location where the peak heating originating from the attachment of the corner vortex can be distinguished from the heating generated by the interaction of the bow shock with the boundary layer.

Figure 30 shows the experimental surface oil flow and the numerical surface streamlines and shear stress magnitude on the plate for the 2.5 mm fin. As for the 7.5 mm fin, there is good agreement between the experimental and numerical results, within the limitations of the method. In particular, the sharply delineated white bands in the photograph showing an accumulation of oil in the experiments lie at edges of the regions of high shear stress in the numerical solution. Similarly, there is a match between the surface oil flow and the numerically generated flow pattern at the surface of the plate for the 5 mm fin (figures 3 and 25).

The off-surface flow was investigated for the 2.5 and 5 mm fins using the numerical solutions. Generally the flow features are consistent for those for the 7.5 mm fin as discussed above in § 4.3. However, there are noticeable fin diameter effects in the

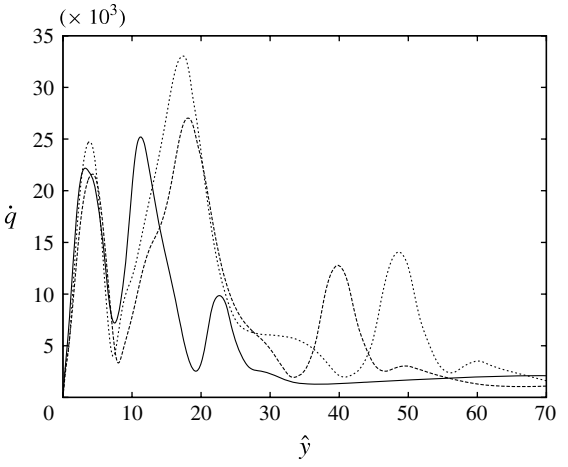

FIGURE 29. Cross-flow normalized surface numerical heat flux in $\mathrm{W\,m^{-2}}$ for different diameter fins; solid line $D = 2.5$ mm at $x = 15.5D$, dashes $D = 5$ mm at $x = 10.5D$, dots $D = 7.5$ mm at $x = 5.5D$. $\hat{y} = y - D/2$ in mm.

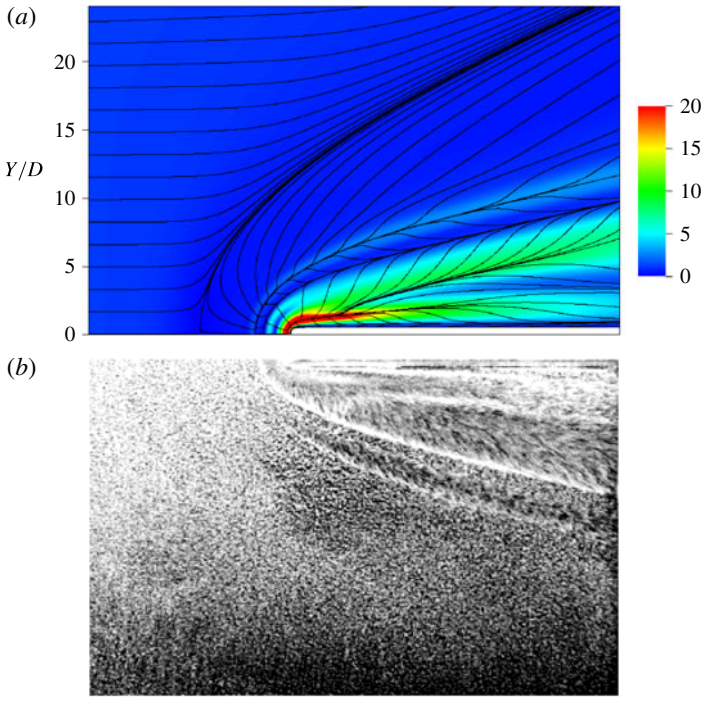

FIGURE 30. (Colour online) Flow pattern on the plate for the $D = 2.5$ mm fin. (*a*) Numerical, surface streamlines and shear stress magnitude (colour) normalized on the flat plate value at the nose of the fin. (*b*) Experimental, surface oil flow. $-14.8 < x/D \leqslant 24$, $0 \leqslant y/D \leqslant 24$.

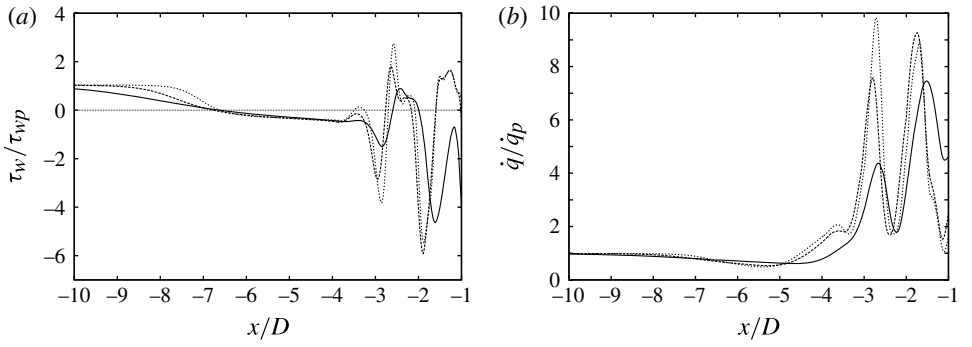

FIGURE 31. (*a*) Wall shear stress and (*b*) heat flux on the symmetry line ahead of the fin for different diameter fins: solid, $D = 2.5$ mm; dashes, $D = 5$ mm; dots, $D = 7.5$ mm. Values are normalized by the local flat plate values.

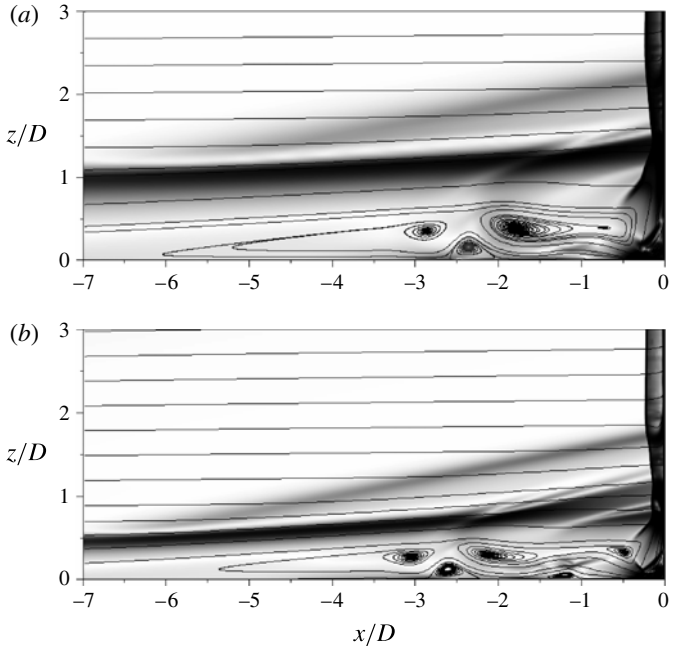

FIGURE 32. Numerical schlieren and streamlines for the flow along the symmetry line upstream of the fin: (*a*) $D = 2.5$ mm; (*b*) $D = 5$ mm.

details of the flow, particularly in the vortical structure. Figure 31 shows the wall shear stress and the surface heat transfer rate on the symmetry line ahead of the fin for all three fins, while figure 32 shows numerical schlierens and streamlines ahead of the fin for $D = 2.5$ and 5 mm. The distributions of τ_w and $\dot{q}$ for all three fins are similar, but for both quantities the size of the peaks increases with the fin diameter, while the vortical structure is generally weaker with a smaller diameter fin. In particular, there are two main cores and secondary shocks for $D = 2.5$ mm, but three for the two larger fins (figures 8 and 32). The position of the main separation point shows little variation,

being at $x/D \approx -6.5$ for all three fins. The apparent large difference in the gradients of τ_w and $\dot{q}$ at separation for different D in figure 31 are due to the scaling with D; in physical terms (i.e. against x rather than X/D) these are similar. The similarity of the flow as it passes through separation is consistent with the free-interaction theory proposed by Chapman, Kuehn & Larson (1957), where the separation depends only on the oncoming flow, which is similar for all three fins. Likewise, the boundary layer thickness for the flow approaching the separation is similar for all three cases in physical terms, but it appears to differ in the schlieren plots (figures 8 and 32) because of the scaling with D. The point of intersection of the primary separation shock with the bow shock contains a mixture of scales so differs both physically and in terms of D. This shock is at the same inclination in all three cases so the position of the intersection point is determined by the boundary layer thickness at the separation point, and the length of the separation region. The former depends primarily on the distance from the leading edge of the plate, not on D, and the latter on D.

Some calculations were performed on paths of particles following the flow. These showed the expected pattern, with particles originating near the symmetry line upstream of the fin–body interaction region being entrained into the separation region and then around the side of the fin in the vortical structure near the plate, as sketched in figure 1. Particles starting near the plate surface in the boundary layer upstream of the interaction region but away from the symmetry line were convected up and over the interaction region, and were displaced laterally as the flow passed the fin. Particles above the interaction region (i.e. above the boundary layer) were displaced upwards and laterally as they travelled downstream past the fin, but some fluid originating near the symmetry line but off the surface travels over the main vortex around the nose of the fin and is then drawn down into the region between the wall of the fin and the bow shock (see the streamlines in figure 19).

6. Summary and conclusions

High-resolution numerical solutions have been obtained for laminar hypersonic flow past a fin with a cylindrical leading edge mounted on a flat plate. The results have been compared with those from complementary experiments performed with the same geometry and flow parameters (Mach and Reynolds numbers). The main quantitative experimental results are maps of the heat flux on the surface of the plate obtained from liquid-crystal thermography. Within the limits of the experiments (accuracy and range of the liquid crystals and uncertainties in the flow conditions) the agreement between the experimental and numerical results is as good as could be expected, in particular, of the pattern of heating on the plate. Comparisons were also made between streamlines (numerical) and oil flow (experimental) on the surface of the plate, and between experimental and numerical schlierens. Again, there was good agreement.

The level of agreement between the numerical and experimental results demonstrates the ability of the numerical method to accurately predict the flow, providing far more detailed information than would be available from experimental measurements alone. This applies in particular to the off-surface flow, but also to the ability to predict surface heating rates, one of the key variables of interest. In general, the highly localized nature of the heating and the rapid response required of the sensors (most hypersonic experimental facilities have a short run time; the 0.5 s here is relatively long), means that it is difficult to obtain accurate measurements of peak heating in an experiment. Note that the flow here is of relatively low enthalpy so that real gas affects, which can have a major effect on hypersonic flow (see chap. 7 of Babinsky & Harvey 2011), are not an issue here.

The agreement between the predictions of the heat transfer rate from the Eckert correlation (2.4) and the numerical and experimental values show that the boundary layer flow is laminar well past separation. Some degree of unsteady or transitional flow in the interaction region ahead of the fin flow cannot be ruled out in the experiments. However, there is no sign of the increase in heat transfer rate that would be expected with turbulent flow in the measurements in this area, which never exceed those from the simulations. Also, the size of the separation region in the experiments agrees well with that obtained from the numerical solutions, being much larger than found in experiments with turbulent flow. The numerical procedure did not assume steady flow, the solutions being time marched to a steady state with no sign of unsteadiness in the flow.

The effect of the fin diameter/thickness was investigated. The basic scale for the fin–body interaction is the the diameter D of the fin. Both numerically and experimentally, the primary separation point along the symmetry line ahead of the fin occurs at the same distance (in terms of D) ahead of the fin for all three fins studied. An exception to the scaling with diameter was the flow in the corner of the fin–plate junction along the side of the fin, which varies with physical distance downstream from the nose of the fin. Also, the flow in the region of the primary separation ahead of the fin varies with physical distance, in accordance with the free-interaction theory (Chapman *et al.* 1957). The separation point on the symmetry line was $6.5D$ ahead of the fin. This is in marked contrast to the turbulent boundary layer case where the separation point is $2D$–$3D$ ahead (Hung & Clauss 1981; Haq 1993). Also, it is shorter than the $9D$–$12D$ found for a cylinder with a Mach 5.3 flow by Hung & Clauss (1981). However, Hung & Clauss (1981) used the drop in heat flux to predict the separation point, and this occurs ahead of the separation as the boundary layer thickens approaching the separation point, as shown in figures 5 and 12. A lower value of $x/D \approx -6.3$ was found experimentally by Özcan & Holt (1984) for a cylinder with laminar flow in a Mach 2.36 flow.

A set of vortical structures, commonly referred to as horseshoe vortices, is generated in the fin–body interaction region. The structure found in the numerical solution on the symmetry line ahead of the fin for the 7.5 mm fin has a separation bubble containing three co-rotating primary cores, with smaller secondary vortices located near the surface between the primary cores, rotating in the opposite sense to the cores. The streamlines passing immediately above the cores have varying curvature, alternately convex and concave, causing a sequence of expansions and compressions, which generate multiple shocks. The vortex structure on the symmetry line wraps around the fin at an oblique angle to it. As the flow proceeds around the fin, the vortices nearest the fin are affected by the bow shock, also at an oblique but larger angle to the fin.

Although the fin–body interaction region is the same size in terms of the fin diameter for all three fins, there are distinct differences in the flow within the separation region, with, in general, a stronger vortical structure within the interaction region for the larger fins.

The pattern of heat flux on the surface of the plate was essentially the same numerically and experimentally for all three fins. However, the liquid crystals had a limited range, and much larger values of heat flux (two orders of magnitude greater than the undisturbed flat plate values) were found in the simulations in regions where it was not possible to gain an accurate (or any) estimate in the experiments. Very sharp peaks were found in the regions of maximum heat flux, particularly on the fin.

Concentrated heating of this kind has been found in previous studies, for example Hiers & Loubsky (1967).

Commonly in studies of this type peak heating rates are associated with shock–shock interactions. However, one perhaps surprising result of this study is the prediction that surface heat fluxes associated with attachments can be at least as large as those generated by shock–shock interactions, with extremely high heat fluxes in the interaction region on the plate as well as on the leading edge of the fin. We note that surface heat fluxes two orders of magnitude greater than the undisturbed flat plate values have been found in experiments for laminar flow past a cylinder at Mach 5.3 (Hung & Clauss 1981), with a pattern of peaking similar to that found in our calculations.

REFERENCES

Amaratunga, S., Tutty, O. R. & Roberts, G. T. 2000 High-speed flow with discontinuous surface catalysis. *J. Fluid Mech.* **420**, 325–359.

Amick, J. L. 1961 Pressure measurements on sharp and blunt 5° and 15° half cone at Mach number 3.86 and angles of attack to 100°. *NASA TN* D-173.

Anderson, J. D. 1989 *Hypersonic and High Temperature Gas Dynamics*. McGraw-Hill.

Anderson, J. D. 1990 *Modern Compressible Flow*. McGraw-Hill.

Babinsky, H. & Harvey, J. K. (Eds) 2011 *Shock Wave–Boundary-Layer Interactions*. Cambridge University Press.

Burcham, F. W. & Nugent, J. 1970 Local flow field around a pylon-mounted dummy ramjet engine on the x-15-2 for Mach numbers 2.0 to 6.7. *NASA TN-D* 5638.

Chapman, D. R., Kuehn, D. M. & Larson, H. K. 1957 Investigation of separated flows in supersonic and subsonic streams with emphasis on the effects of transition. *NACA-TR*-1356.

Delery, J. & Marvin, J. G. 1986 Shockwave boundary layer interactions. *AGARD-AG*-280.

Dolling, D. S. & Bogdanoff, S. M. 1981 Scaling of interactions of cylinders with supersonic turbulent boundary layers. *AIAA J.* **19**, 655–657.

Dolling, D. S. & Bogdanoff, S. M. 1982 Blunt fin-induced shock wave/turbulent boundary layer interaction. *AIAA J.* **20**, 1674.

Dolling, D. S. & Bogdanoff, S. M. 2001 Fifty years of shock-wave/boundary layer research? What next? *AIAA J.* **39**, 1517.

Eckert, E. R. G. 1955 Engineering relations for skin friction and heat transfer to surfaces in high velocity flows. *J. Aerosp. Sci.* **22**, 585–587.

Edney, B. E. 1968 Anomolous heat transfer and pressure distributions on blunt bodies at hypersonic speeds in the presence of an impinging shock. *Tech. Rep.* 115. FFA (Aeronautical Research Council of Sweden).

Fay, J. A. & Riddell, F. R. 1958 Theory of stagnation point heat transfer in dissociated air. *J. Aeronaut. Sci.* **25**, 73–85.

Haq, Z. U. 1993 Hypersonic vehicle interference heating. PhD thesis, Univ. of Southampton, Dept. of Aeronautics and Astronautics, Southampton, England.

Haq, Z., Roberts, G. T. & East, R. A. 1991 Interference heating near fin/body junctions on hypersonic vehicles. In *Proceedings of the First European Symposium on Aerothermodynamics for Space Vehicles*, pp. 171–176. European Space Agency SP-318.

Hayes, W. D. & Probstein, R. F. 1959 *Hypersonic Flow Theory*. Academic.

Hiers, R. S. & Loubsky, W. L. 1967 Effects of shockwave impingement on the heat transfer on a cylindrical leading edge. *NASA TN-D* 3859.

Holden, M. S. 1986 A review of aerothermal problems associated with hypersonic flight. *AIAA Paper* 86-0267.

Houwing, A. F. P., Smith, D. R., Fox, J. S & Mudford, N. R. 2001 Laminar boundary layer separation at a fin-body junction in a hypersonic flow. *Shock Waves* **11**, 31.

HUNG, C. M. & BUNING, P. G. 1985 Simulation of blunt-fin-induced shock-wave and turbulent boundary-layer interaction. *J. Fluid Mech.* **154**, 163.

HUNG, F. T. & CLAUSS, J. M. 1981 Three-dimensional protuberance interference heating in high speed flow. *Prog. Aeronaut. Astronaut.* **77**, 109–136.

LAKSHMANAN, B. & TIWARI, S. N. 1994 Investigation of three-dimensional separation at wing/body junctions in supersonic flows. *AIAA J. Aircraft* **31**, 64.

van LEER, B. 1979 Towards the ultimate conservative scheme v. A second-order sequel to Godunov. *J. Comput. Phys.* **32**, 101–136.

NAVARRO-MARTINEZ, S. 2002 Numerical simulation of laminar flow over hypersonic compression ramps. PhD thesis, University of Southampton.

NAVARRO-MARTINEZ, S. & TUTTY, O. R. 2005 Numerical simulation of Görtler vortices in hypersonic compression ramps. *Comput. Fluids* **34**, 225–247.

ÖZCAN, O. & HOLT, M. 1984 Supersonic separated flow past a cylindrical obstacle on a flat plate. *AIAA J.* **22**, 611–617.

QASWARI, A. M. S. 1977 Measurement of hypersonic dynmic stability of pitching blunt-nosed bodies in a short duration facility. PhD thesis, Univ. of Southampton, Dept. of Aeronautics and Astronautics, Southampton, England.

QUIRK, J. J. 1994 A contribution to the great Riemann solver debate. *Intl J. Numer. Meth. Fluids* **18**, 555–574.

ROBERTS, G. T. & EAST, R. A. 1996 Liquid crystal thermography for heat transfer measurement in hypersonic flows: a review. *J. Spacecr. Rockets* **33**, 761–768.

ROBERTS, G. T., SCHURICHT, P. H. & MUDFORD, N. R. 1998 Heating enhancement caused by a transverse control jet in hypersonic flow. *Shock Waves* **8**, 105–112.

RUSANOV, V. V. 1961 Calculation of interaction of non-steady shock waves with obstacles. *J. Comput. Math. Phys. USSR* **1**, 267–279.

SCHULTZ, D. L. & JONES, T. V. 1973 Heat transfer measurements in short-duration hypersonic facilities. *AGARD-AG*-165.

SCHURICHT, P. H. & ROBERTS, G. T. 1998 Hypersonic interference heating induced by a blunt fin. *AIAA Paper* 98-1579.

SHANKAR, P. N. & DESHPANDE, M. D. 2000 Fluid mechanics in the driven cavity. *Annu. Rev. Fluid Mech.* **32**, 93–136.

STOLLERY, J. L. 1989 Glancing shock-boundary layer interactions. *AGARD-R*-764.

TORO, E. F., SPRUCE, M. & SPEARES, W. 1994 Restoration of the contact surface on the hll-Riemann solver. *Shock Waves* **4**, 25–34.

TUTTY, O. R., ROBERTS, G. T., EAST, R. A. & HUNTINGTON-THRESHER, W. 1994 Numerical study of fin-body interference effects at hypersonic speeds. In *Proceedings of 2nd European Symposium on Aerothermodynamics for Space Vehicles,* vol. ESA SP-367, p. 51.

YAO, Y., SANDHAM, N. D. & ROBERTS, G. T. 2007 The effect of Mach number on unstable disturbances in shock/boundary-layer interactions. *Phys. Fluids* **19**, 054104.